Perivascular NOTCH3$^+$ Stem Cells Drive Meningioma Tumorigenesis and Resistance to Radiotherapy

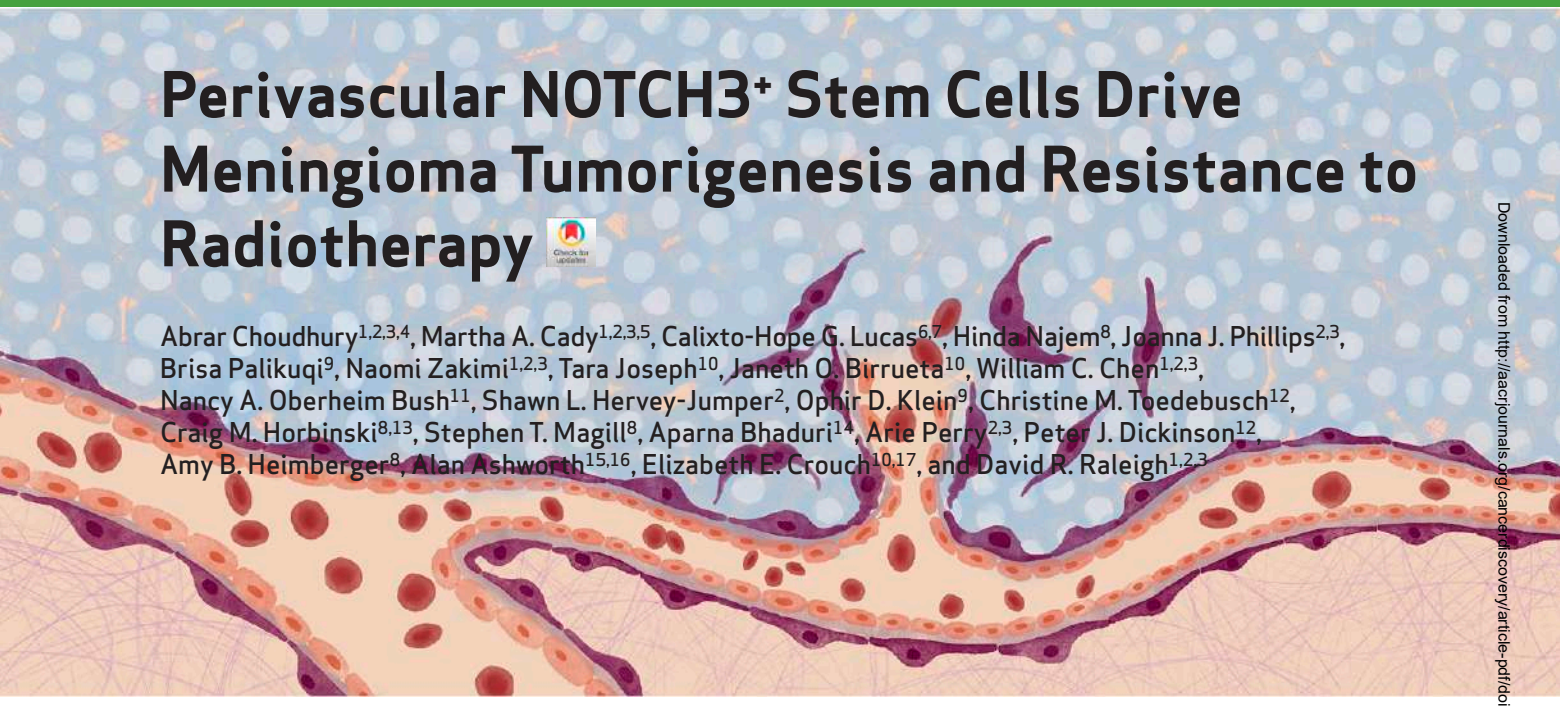

Abrar Choudhury[1,2,3,4], Martha A. Cady[1,2,3,5], Calixto-Hope G. Lucas[6,7], Hinda Najem[8], Joanna J. Phillips[2,3], Brisa Palikuqi[9], Naomi Zakimi[1,2,3], Tara Joseph[10], Janeth O. Birrueta[10], William C. Chen[1,2,3], Nancy A. Oberheim Bush[11], Shawn L. Hervey-Jumper[2], Ophir D. Klein[9], Christine M. Toedebusch[12], Craig M. Horbinski[8,13], Stephen T. Magill[8], Aparna Bhaduri[14], Arie Perry[2,3], Peter J. Dickinson[12], Amy B. Heimberger[8], Alan Ashworth[15,16], Elizabeth E. Crouch[10,17], and David R. Raleigh[1,2,3]

ABSTRACT

Meningiomas are the most common primary intracranial tumors. Treatments for patients with meningiomas are limited to surgery and radiotherapy, and systemic therapies remain ineffective or experimental. Resistance to radiotherapy is common in high-grade meningiomas and the cell types and signaling mechanisms that drive meningioma tumorigenesis and resistance to radiotherapy are incompletely understood. Here, we report that NOTCH3 drives meningioma tumorigenesis and resistance to radiotherapy and find that perivascular NOTCH3$^+$ stem cells are conserved across meningiomas from humans, dogs, and mice. Integrating single-cell transcriptomics with lineage tracing and imaging approaches in genetically engineered mouse models and xenografts, we show NOTCH3 drives tumor-initiating capacity, cell proliferation, angiogenesis, and resistance to radiotherapy to increase meningioma growth and reduce survival. To translate these findings to patients, we show that an antibody stabilizing the extracellular negative regulatory region of NOTCH3 blocks meningioma tumorigenesis and sensitizes meningiomas to radiotherapy, reducing tumor growth and improving survival.

SIGNIFICANCE: There are no effective systemic therapies to treat meningiomas, and meningioma stem cells are poorly understood. Here, we report perivascular NOTCH3$^+$ stem cells to drive meningioma tumorigenesis and resistance to radiotherapy. Our results identify a conserved mechanism and a therapeutic vulnerability to treat meningiomas that are resistant to standard interventions.

[1]Department of Radiation Oncology, University of California San Francisco, San Francisco, California. [2]Department of Neurological Surgery, University of California San Francisco, San Francisco, California. [3]Department of Pathology, University of California San Francisco, San Francisco, California. [4]Medical Scientist Training Program, University of California San Francisco, San Francisco, California. [5]Tetrad Graduate Program, University of California San Francisco, San Francisco, California. [6]Department of Pathology, Johns Hopkins University, Baltimore, Maryland. [7]Department of Neurosurgery, Johns Hopkins University, Baltimore, Maryland. [8]Department of Neurological Surgery, Northwestern University, Chicago, Illinois. [9]Department of Orofacial Sciences, University of California San Francisco, San Francisco, California. [10]Department of Pediatrics, University of California San Francisco, San Francisco, California. [11]Department of Neurology, University of California San Francisco, San Francisco, California. [12]Department of Surgical and Radiological Sciences, School of Veterinary Medicine, University of California Davis, Davis, California. [13]Department of Pathology, Northwestern University, Chicago, Illinois. [14]Department of Biological Chemistry, University of California Los Angeles, Los Angeles, California. [15]Department of Medicine, University of California San Francisco, San Francisco, California. [16]Helen Diller Family Comprehensive Cancer Center, University of California San Francisco, San Francisco, California. [17]The Eli and Edythe Broad Center of Regeneration Medicine and Stem Cell Research, University of California San Francisco, San Francisco, California.

A. Choudhury and M.A. Cady contributed equally to this article.

Corresponding Author: David R. Raleigh, 1450 3rd Street, HD481, San Francisco, CA 94158. E-mail: david.raleigh@ucsf.edu

Cancer Discov 2024;XX:1–15

doi: 10.1158/2159-8290.CD-23-1459

INTRODUCTION

Meningiomas arising from the meningothelial lining of the central nervous system comprise more than 40% of primary intracranial tumors (1–3), and approximately 1% of humans will develop a meningioma in their lifetime (4). The World Health Organization (WHO) grades meningiomas according to histologic features such as mitotic count and rare molecular alterations that are associated with poor clinical outcomes (1). Surgery and radiotherapy are the mainstays of meningioma treatment (5), and most WHO grade 1 meningiomas can be effectively treated with standard interventions but many WHO grade 2 or WHO grade 3 meningiomas are resistant to treatment and cause neurologic morbidity and mortality (6). All clinical trials of systemic therapy have failed to durably block meningioma growth or improve survival (6, 7), and conserved, targetable mechanisms underlying aggressive meningiomas are elusive.

Recent bioinformatic investigations have shed light on meningioma biology, revealing molecular groups of tumors with distinct clinical outcomes that provide a framework for investigating meningioma resistance to treatment (8–15). DNA methylation profiling shows that meningiomas are comprised of Merlin-intact, immune-enriched, and hypermitotic molecular groups (8), which can be divided into subgroups that are concordant across different approaches for meningioma molecular classification (10, 13, 14). Merlin-intact meningiomas encode at least one wild-type copy of the tumor suppressor *NF2* on chromosome 22q, typically have favorable clinical outcomes, and are sensitive to cytotoxic treatments such as radiotherapy (8, 16). In contrast, immune-enriched and hypermitotic meningiomas can have biallelic inactivation of *NF2* and usually have intermediate or poor clinical outcomes, including resistance to radiotherapy (8, 16, 17). Associations between loss of one versus two copies of *NF2* across WHO grades of meningiomas are limited, suggesting that molecular grouping may shed light on therapeutic vulnerabilities that drive meningioma resistance to standard interventions.

Cancer stem cells can mediate resistance to radiotherapy (18), but the cell types and signaling mechanisms driving tumorigenesis or resistance to radiotherapy across molecular groups of meningiomas are unknown. Morphologic correlates between meningioma cells and arachnoid cap cells found on meningeal invaginations of dural venous sinuses have fueled a longstanding and widely accepted hypothesis that meningiomas arise from the arachnoid cap (19, 20). However, the WHO recognizes 15 histologic variants of meningiomas (1), most of which do not resemble arachnoid cap cells or which may develop far from dural venous sinuses, including rare cases of primary intraparenchymal, intraventricular, or pulmonary meningiomas (21–23). These data suggest other cell types may contribute to meningioma tumorigenesis, and that understanding the cell types and signaling mechanisms that drive meningioma tumorigenesis or resistance to radiotherapy may reveal new targets for systemic therapies to treat patients with meningiomas.

RESULTS

NOTCH3 Is Enriched in Meningioma Mural Cells and Is Expressed throughout High-Grade Meningiomas

To elucidate the cellular architecture of meningiomas and distinguish single tumor cell states from single tumor microenvironment cell types, single-cell RNA sequencing was performed on 30,934 cells from six human meningioma samples with loss of at least one copy of chromosome 22q (Fig. 1A; Supplementary Fig. S1A). Datasets were integrated and corrected for batch effects using Harmony (Supplementary Fig. S1B; ref. 24), and Uniform Manifold Approximation and Projection for Dimension Reduction (UMAP) revealed a total of 13 cell clusters that were defined using automated cell type classification (25), cell signature gene sets (26), cell cycle analysis, and differentially expressed cluster marker genes (Supplementary Table S1). Reduced dimensionality clusters of meningioma tumor cells with loss of chromosome 22q were distinguished from microenvironment cells using CONICS (Fig. 1B; Supplementary Fig. S1C; ref. 27). The majority of meningioma cell clusters grouped together in UMAP space, including meningioma cells expressing cell cycle genes (C0, C3, and C4), signal transduction genes (C1), or extracellular matrix remodeling genes (C10; Fig. 1A; Supplementary Fig. S1D–S1G; Supplementary Table S1). Three meningioma cell clusters with loss of chromosome 22q did not group with other meningioma cell types and were distinguished by expression of mural cell markers (C7, C11, and C12), including genes associated with pericytes (*CD248*, *ABCC9*, *CSPG4*, and *GJA4*), fibroblasts (*SERPING1* and *CLU*), smooth muscle cells (*SDC2* and *ACTA2*), and multiple mural cell lineages (*PDGRFB* and *RGS5*; Fig. 1A–C; Supplementary Fig. S1F; Supplementary Table S1; refs. 28–30). The cluster of cells expressing endothelial markers (C8), including genes associated with tip cells (*ADM*, *ANGPT2*, and *COL9A3*), capillary cells (*MFSD2A*), arterial cells (*CXCL12*), and multiple endothelial cell lineages (*CD34*, *VWF*, *CLDN5*, *PECAM1*, *PDGFD*, *KDR*, *FLT*, *FLT1*, and *TIE1*; refs. 28–30) did not show loss of chromosome 22q (Fig. 1A–C; Supplementary Fig. S1F; Supplementary Table S1).

Meningioma mural cell clusters were distinguished from one another by expression of cell cycle genes (*MKI67*, *TOP2A*, and *AURKB*) or cancer stem cell genes (*NOTCH3* and *THY1*; Fig. 1C; refs. 31–33). The cluster of meningioma mural cells that was enriched in *NOTCH3* and *THY1* (C11), as well as the endothelial cell cluster (C8), also expressed NOTCH ligands (*JAG1*, *JAG2*, *DLL1*, *DLL4*, and *FN1*; Fig. 1C). Cell–cell communication analysis of single-cell RNA sequencing data using CellChat (34) suggested that the NOTCH signaling network was active in meningiomas with loss of at least one copy of chromosome 22q, particularly among and between NOTCH3$^+$ meningioma mural cells and endothelia (Fig. 1D). *NOTCH3* was also expressed in other meningioma cell clusters that were marked by the meningioma gene *SSTR2A* (Supplementary Fig. S1G; ref. 35), but other NOTCH receptors were not expressed across meningioma cell types (Supplementary Table S1).

The evolutionarily conserved NOTCH family of transmembrane proteins enables intercellular communication to regulate mammalian cell fate and growth (36–38). Similar to humans, the most common primary intracranial tumors in

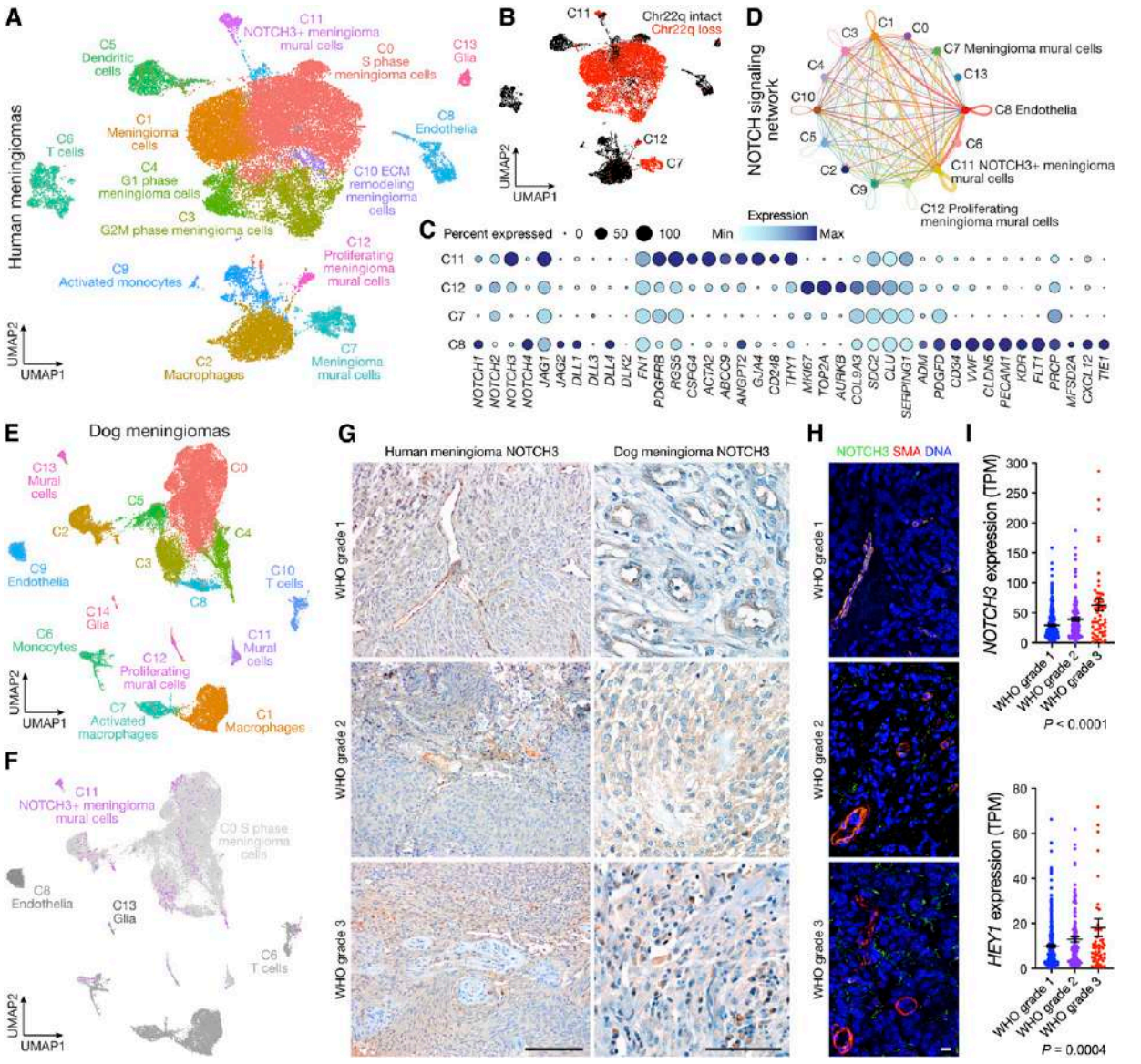

Figure 1. NOTCH3 is enriched in meningioma mural cells and is expressed throughout high-grade meningiomas. **A,** Single-cell RNA sequencing UMAP of 30,934 transcriptomes from human meningioma samples with loss of chromosome 22q showing tumor cell states and microenvironment cell types. **B,** UMAP showing single-cell RNA sequencing of human meningiomas shaded by chromosome 22q status. **C,** Dot plot showing expression of NOTCH receptors (*NOTCH1*, *NOTCH2*, *NOTCH3*, and *NOTCH3*), NOTCH ligands (*JAG1*, *JAG2*, *DLL1*, *DLL3*, *DLL4*, *DLK2*, and *FN1*), mural cell markers (*PDGFRB*, *RGS5*, *CSPG4*, *ACTA2*, *ABCC9*, *ANGPT2*, *GJA4*, *CD248*, *COL9A3*, *SDC2*, *CLU*, and *SERPING1*), cancer stem cell marker (*NOTCH3*, and *THY1*), cell proliferation markers (*MKI67*, *TOP2A*, and *AURKB*), and endothelial cells markers (*ADM*, *PDGFD*, *CD34*, *VWF*, *CLDN5*, *PECAM1*, *KDR*, *FLT1*, *PRCP*, *MFSD2A*, *CXCL12*, and *TIE1*) across meningioma mural (C7, C11, and C12) or endothelial cells (C8) from **A**. **D,** Inference of NOTCH signaling network in human meningiomas using single-cell RNA sequencing cell–cell communication analysis. **E,** Single-cell RNA sequencing UMAP of 40,525 dog meningioma transcriptomes showing tumor cell states and microenvironment cell types. **F,** Transcriptomic concordance of human meningioma single-cell cluster identities from **A** projected on single-cell RNA sequencing UMAP of 40,525 transcriptomes from dog meningioma samples showing NOTCH3⁺ meningioma mural cells and proliferating meningioma cells are conserved across human and dog meningiomas. **G,** IHC for NOTCH3 across histologic grades of human (top) or dog (bottom) meningiomas. Representative of $n = 10$ meningiomas per grade. Scale bars, 100 μm. **H,** IF for NOTCH3 and the mural cell marker SMA across histologic grades of human meningiomas. DAPI marks DNA. Representative of $n = 10$ meningiomas per grade. Scale bars, 10 μm. **I,** Quantification of *NOTCH3* or the NOTCH3 target gene *HEY1* across meningioma grades using RNA sequencing of $n = 502$ human meningiomas. TPM, transcripts per million. Lines represent means and error bars represent standard error of means. ANOVA.

dogs are meningiomas (39). To determine if NOTCH3⁺ meningioma mural cells were conserved in meningiomas from other mammals, single-cell RNA sequencing was performed on 40,525 cells from five dog meningioma samples (Supplementary Fig. S2A). Datasets were integrated and corrected for batch effects using Harmony (Supplementary Fig. S2B; ref. 24), and UMAP revealed a total of 14 cell clusters that were defined using automated cell type classification (25), cell signature gene sets (26), cell cycle analysis (Fig. 1E; Supplementary Fig. S2C), and differentially expressed cluster marker

genes (Supplementary Fig. S2D and S2E; Supplementary Table S2). Human meningioma single-cell cluster identities were projected onto reduced dimensionality clusters of dog meningioma cells using transcriptional correlation and expression of conserved marker genes across species, revealing conservation of endothelia, glia, and immune cell types in the tumor microenvironment (Fig. 1F). The NOTCH3$^+$ human meningioma mural cell cluster identities mapped to both a unique dog meningioma mural cell cluster and in a mixed cluster that was comprised of cycling meningioma cells (Fig. 1F). These data suggest that NOTCH3$^+$ meningioma mural cells are conserved across mammalian meningiomas.

Meningiomas in humans and dogs share similar histologic features (Supplementary Fig. S2F), and IHC for NOTCH3 across all grades of human or dog meningiomas showed NOTCH3 was heterogeneous and predominantly restricted to the perivascular niche in low-grade meningiomas but was expressed throughout high-grade meningiomas from both species (Fig. 1G; Supplementary Fig. S3A–S3C). Semiquantitative analysis of human NOTCH3 immunoreactivity revealed expression increased in areas of the cellular tumor across WHO grades, but the expression in the perivascular niche did not. Indeed, intensity (P = 0.7496), extent (P = 0.6082), and total NOTCH3 staining (P = 0.6822) were equivalent in the perivascular niche across WHO grades (ANOVA), but NOTCH3 expression increased in intensity (P = 0.0409), extent (P = 0.0113), and total staining (P = 0.0035) in areas of cellular tumor from WHO grade 1 (n = 10) to WHO grade 2 (n = 10) to WHO grade 3 (n = 10) meningiomas (ANOVA). Immunofluorescence (IF) of the same human meningiomas across all grades demonstrated that NOTCH3 was expressed by mural cells marked by SMA (*ACTA2*) and was enriched throughout high-grade meningiomas but was not expressed by endothelial cells marked by VWF (Fig. 1H; Supplementary Fig. S4–S9). In support of these data, reanalysis of RNA sequencing of 502 human meningiomas (8, 10) showed that expression of *NOTCH3* and the NOTCH3 target gene *HEY1* increased from WHO grade 1 (n = 329) to WHO grade 2 (n = 117) to WHO grade 3 (n = 56) meningiomas (Fig. 1I).

NOTCH3$^+$ Mural Cells Underlie Meningeal Hyperproliferation

The functional relevance of NOTCH3 in meningeal development, homeostasis, and tumorigenesis is unknown, but *NOTCH3* inactivating mutations in humans cause CADASIL (40), a hereditary adult-onset cerebral arteriopathy that is associated with subcortical ischemic events and alterations in brain vascular smooth muscle cells (41). Given the frequent repurposing of developmental pathways in cancer (18), we sought to compare the expression and localization of NOTCH3 in meningeal development, homeostasis, and tumorigenesis. IF of the developing human cortex from gestational week 17 showed NOTCH3 was expressed by mural cells marked by PDGFRβ in the cortical plate and margin zone (Supplementary Fig. S10A), both of which contribute to meningeal development (42–45). Reanalysis of single-cell RNA sequencing data from perinatal human brain vasculature (139,134 cells from gestational weeks 15, 17, 18, 20, 22, and 23; ref. 28) or from adult human brain vasculature (136,161 cells from two studies; refs. 29, 30) demonstrated *NOTCH3* was enriched in mural cells marked by *PDGFRβ* or *ACTA2* (SMA; Supplementary Fig. S10B–S10D). In contrast to *NOTCH3* expression in brain vasculature and meningioma mural cells (Fig. 1C), IHC and IF of adult human meninges showed NOTCH3 expression was restricted to mural cells that were adjacent to (but non-overlapping with) vascular smooth muscle cells expressing SMA (Fig. 2A and B). Thus, NOTCH3$^+$ mural cells in the brain (Supplementary Fig. S10A–S10D), meninges (Fig. 2A and B), and meningiomas (Fig. 1; Supplementary Fig. S1–S9) have partially overlapping gene and protein expression programs, suggesting that these cell types may fulfill different intracranial functions, particularly during meningeal development, homeostasis, or tumorigenesis.

To determine if NOTCH3$^+$ cells give rise to other cell types during meningeal development or homeostasis, a tamoxifen-inducible *Notch3-Cre^{ERT2}* allele (46) was combined with the global double-fluorescent *ROSA$^{mT/mG}$* Cre reporter allele (Fig. 2C; ref. 47). Fluorophore recombination was induced during meningeal development (E16.5) or homeostasis (P30 and P90) and confocal microscopy of whole mount mouse meningeal samples from the cerebral convexities revealed NOTCH3$^+$ cells were restricted to the perivascular niche across all contexts (Fig. 2D and E). PTGDS has been proposed as a marker of meningioma progenitor cells (48), and although *PTGDS* was only expressed in a subset of single cells from our study (Supplementary Fig. S1G), *PTGDS* is more broadly expressed throughout single-cell clusters from Merlin-intact meningiomas (49). Fluorescent lineage tracing using a *Ptgds-Cre* allele (48) and *ROSA$^{mT/mG}$* showed PTGDS cells were not restricted to the perivascular stem cell nice in the mouse meninges from the cerebral convexities (Supplementary Fig. S11).

To determine if NOTCH3$^+$ cells contribute to meningeal cell proliferation, the *Notch3-Cre^{ERT2}* allele was combined with *Nf2$^{fl/fl}$* alleles for conditional biallelic inactivation of the *Nf2* tumor suppressor in mice (50). *Nf2* was inactivated in NOTCH3$^+$ cells *in utero* (E16.5) or in adulthood (P30), and mice were monitored without evidence of neurologic symptoms or other overt phenotypes for 1 year (Fig. 2F). Morphologic examination of the central nervous system after 1 year revealed meningeal hyperproliferation after biallelic inactivation of *Nf2* in NOTCH3$^+$ cells compared with mice with intact *Nf2*, after either *in utero* or adulthood recombination (Fig. 2G). These data support the hypothesis that NOTCH3$^+$ mural cells underlie meningeal hyperproliferation and may contribute to meningeal tumorigenesis (Fig. 2D and E).

NOTCH3 Signaling Drives Meningioma Tumor Initiating Capacity, Cell Proliferation, and Angiogenesis

To identify preclinical reagents for mechanistic and functional interrogation of NOTCH3 signaling in the context of meningioma tumorigenesis, reference transcriptomic signatures of human meningioma single-cell clusters (Fig. 1A) were used to estimate the proportion of NOTCH3$^+$ meningioma mural cells across 502 human meningiomas with matched RNA sequencing and DNA methylation profiling (8, 10). Immune-enriched meningiomas are distinguished from

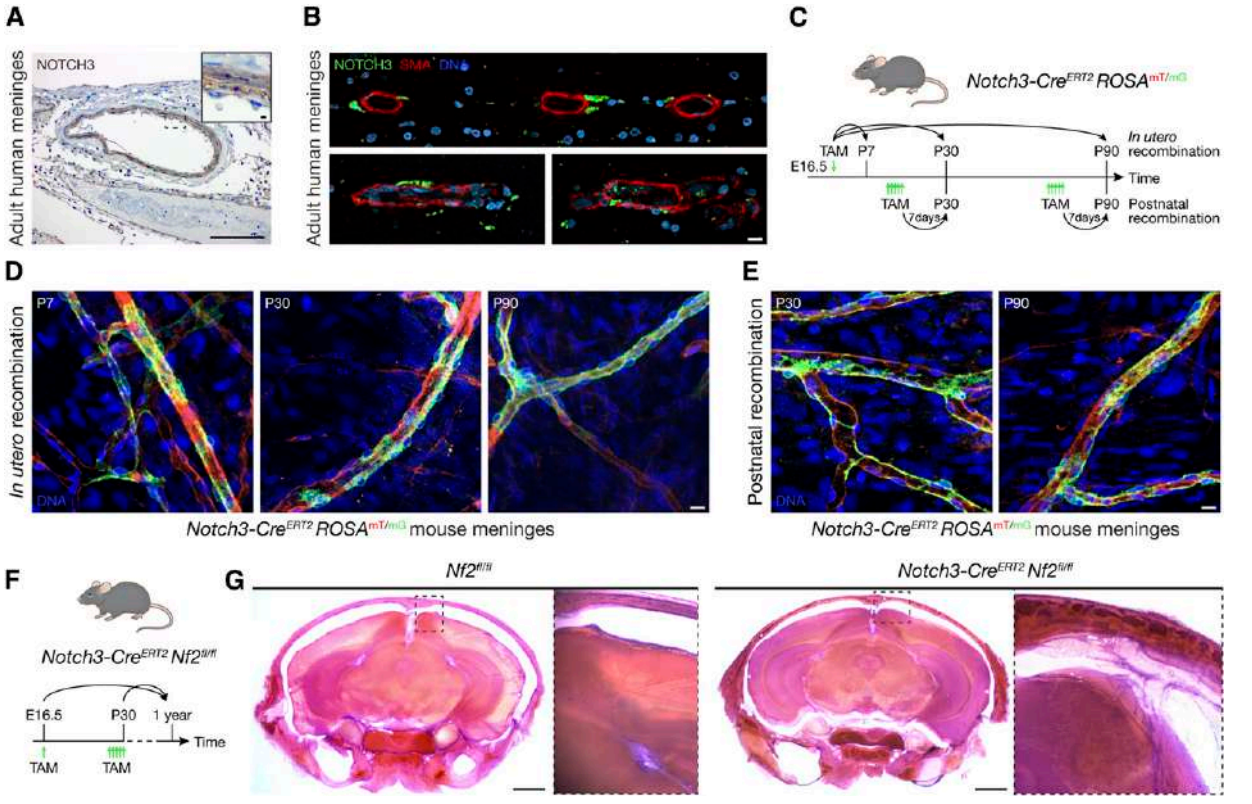

Figure 2. NOTCH3⁺ mural cells underly meningeal hyperproliferation. **A,** IHC for NOTCH3 in the adult human meninges showing expression is restricted to mural cells. Representative of $n = 3$ biological replicates. Scale bars, 100 and 10 μm (insert). **B,** IF for NOTCH3 and the mural cell marker SMA in three adult human meningeal samples showing NOTCH3 is expressed in mural cells adjacent to smooth muscle cells in the meninges. DAPI marks DNA. Scale bar, 10 μm. **C,** Experimental design for *in vivo* lineage tracing of NOTCH3⁺ mural cells during meningeal development (*in utero* recombination) or homeostasis (postnatal recombination). TAM, tamoxifen. **D,** Confocal microscopy of whole mount mouse convexity meningeal samples at P7, P30, or P90 after *in utero* recombination of the *ROSA*$^{mT/mG}$ allele showing NOTCH3 cells (green) are restricted to the perivascular niche during meningeal development. Representative of $n = 3$ biological replicates per timepoint. DAPI marks DNA. Scale bar, 10 μm. **E,** Confocal microscopy of whole mount mouse convexity meningeal samples at P30 or P90 after postnatal recombination of the *ROSA*$^{mT/mG}$ allele showing NOTCH3⁺ cells (green) are restricted to the perivascular niche during meningeal homeostasis. Representative of $n = 3$ biological replicates per timepoint. DAPI marks DNA. Scale bar, 10 μm. **F,** Experimental design for *in vivo* biallelic inactivation of *Nf2* in NOTCH3⁺ cells during meningeal development (E16.5) or homeostasis (P30). Mice were monitored for 1 year after *Nf2* inactivation. **G,** Coronal H&E images of 300 μm decalcified mouse skull sections 1 year after postnatal (P30) treatment of mice with TAM. No gross tumors were identified, but insets show that *Nf2* inactivation in NOTCH3⁺ cells are associated with meningeal hyperproliferation. The same results were obtained after *in utero* (E16.5) treatment with TAM. Representative of $n = 5$–8 biological replicates per condition. Scale bars 1 mm.

other molecular groups by hypomethylation of vascular genes (8), and cell type deconvolution across meningioma DNA methylation groups showed immune-enriched meningiomas (n = 180) were enriched in NOTCH3⁺ meningioma mural cells compared with Merlin-intact (n = 176) or hypermitotic meningiomas (n = 146; Fig. 3A). Immunoblots demonstrated that NOTCH3 was enriched in CH-157MN (51) and IOMM-Lee (52) meningioma cell lines but not in BenMen cells that were derived from a WHO grade 1 meningioma (Fig. 3B; ref. 53). DNA methylation analyses demonstrate that CH-157MN and IOMM-Lee cells classify as immune-enriched, and BenMen cells classify as hypermitotic (8).

NOTCH receptor activation requires ADAM protease cleavage of the extracellular negative regulatory region (NRR), intramembrane proteolysis by the γ-secretase complex, and release of the NOTCH intracellular domain (ICD) that regulates mammalian cell fate and growth (36–38). Small molecule inhibitors of ADAM or γ-secretase do not distinguish between individual NOTCH receptors and have not been adopted in routine clinical practice due to toxicity, but antibody stabilization of the NRR allows for selective inhibition of individual NOTCH receptors in preclinical models (54). An antibody selectively stabilizing the NRR of NOTCH3 (αNRR3; ref. 55) attenuated *in vivo* tumor-initiating capacity (Fig. 3C), blocked expression of *HEY1* (Fig. 3D), and reduced cell proliferation of CH-157MN xenografts (Fig. 3E). Moreover, αNRR3 blocked tumor growth and improved survival of CH-157MN (Fig. 3F) and IOMM-Lee xenografts (Fig. 3G) compared with isotype control treatment or treatment with αNRR1. Overexpression of the NOTCH3 ICD (NOTCH3^{ICD}) increased expression of *HEY1* and PTPRZ1, a marker of meningioma self-renewal (56), and increased clonogenic growth of CH-157MN cells *in vitro* compared with CH-175MN cells expressing empty vector (EV) control (Fig. 3H–J). NOTCH3^{ICD} increased the tumor-initiating capacity of CH-157MN cells using *in vivo* limiting dilution assays (Fig. 3K), and increased tumor growth and reduced survival of CH-157MN xenografts compared with EV (Fig. 3L). Meningiomas are not protected

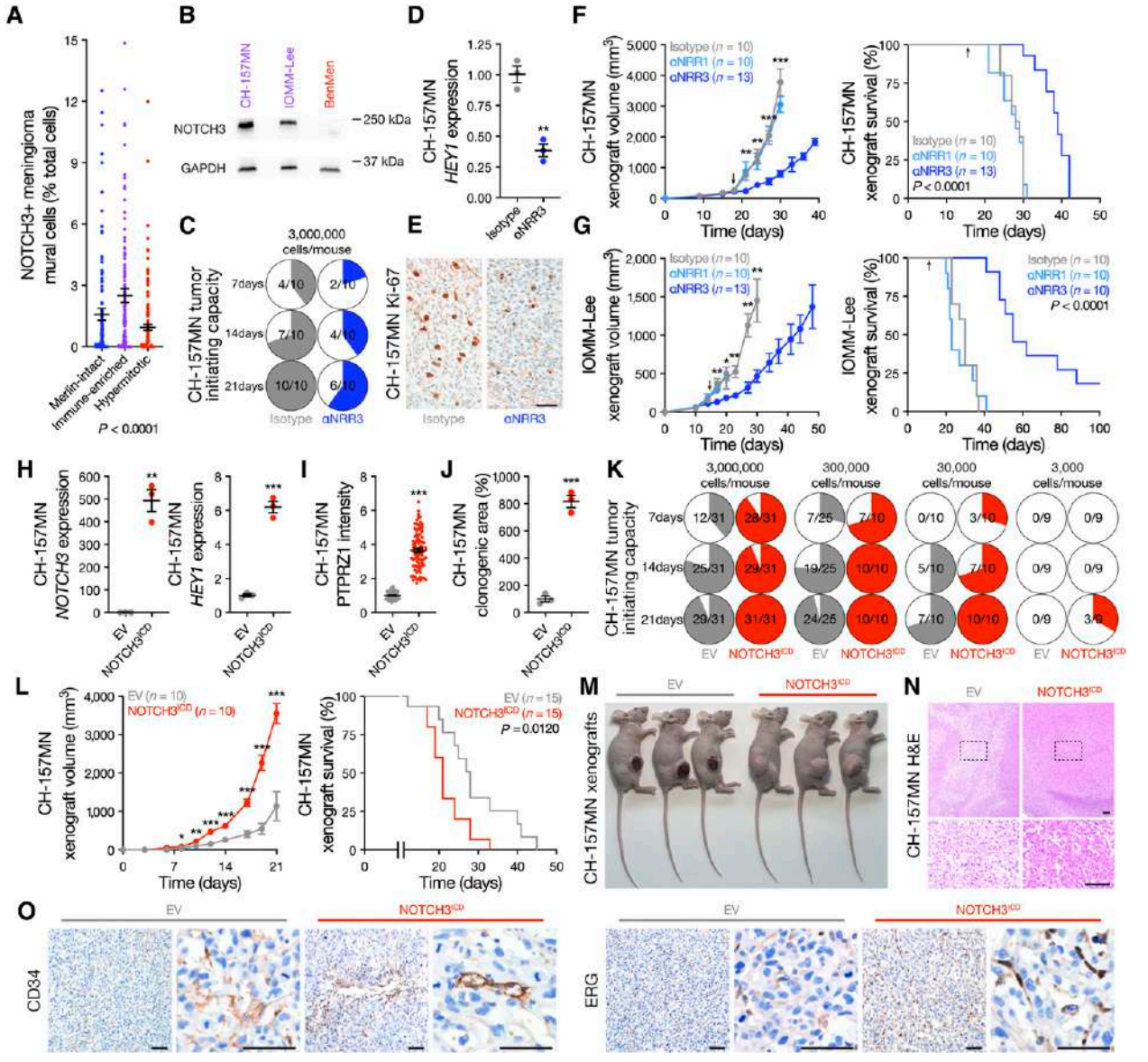

Figure 3. NOTCH3 signaling drives meningioma tumor-initiating capacity, cell proliferation, and angiogenesis. **A,** Deconvolution of NOTCH3$^+$ meningioma mural cells from Fig. 1A using human meningiomas with paired RNA sequencing and DNA methylation profiling ($n = 502$). ANOVA. **B,** Immunoblots showing NOTCH3 is expressed in CH-157MN and IOMM-Lee Immune-enriched meningioma cells but is suppressed in BenMen hypermitotic meningioma cells. **C,** *In vivo* tumor-initiating capacity of CH-157MN meningioma cells in NU/NU mice ± αNRR3 IP injection two times per week. Denominators indicate the number of mice at each time point. Numerators indicate the number of mice with tumors at each time point. **D,** QPCR for the NOTCH3 target gene *HEY1* from meningioma xenografts ± αNRR3 treatment for 2 weeks. Student's *t*-test. **E,** IHC for Ki-67 in meningioma xenografts showing αNRR3 blocks meningioma cell proliferation. Representative of $n = 3$ xenografts per condition. Scale bar, 100 μm. **F,** CH-157MN meningioma xenograft growth (left, Student's *t*-tests) or survival (log-rank test). Arrows indicate the initiation of biweekly treatment with the indicated therapy, which continued until death. **G,** IOMM-Lee meningioma xenograft growth (left, Student's *t*-tests) or survival (log-rank test). Arrows as in **F**. **H,** QPCR for *NOTCH3* or *HEY1* in CH-157MN meningioma cells ± stable expression of EV or NOTCH3^{ICD}. Student's *t*-tests. **I,** IF quantification of the stem cell marker PTPRZ1 in CH-157MN meningioma cells. Student's *t*-test. **J,** Clonogenic *in vitro* growth of CH-157MN meningioma cells after 2 weeks. Student's *t*-test. **K,** *In vivo* tumor-initiating capacity of CH-157MN meningioma cells ± EV or NOTCH3^{ICD} over limiting dilutions. Numerator and denominator as in **C**. **L,** CH-157MN meningioma xenograft growth (left, Student's *t*-tests) or survival (log-rank test). **M,** Images of heterotopic meningioma xenografts showing macroscopic necrosis and ulceration in EV meningiomas. Representative of $n = 7$–9 xenografts per condition. **N,** H&E low and high (box) magnification images of meningioma xenografts showing microscopic necrosis in EV meningiomas. Representative of $n = 3$ xenografts per condition. Scale bars, 100 μm. **O,** IHC for endothelial markers in meningioma xenografts showing NOTCH3^{ICD} induces meningioma angiogenesis. Representative of $n = 3$ xenografts per condition. Scale bars, 100 μm. Lines represent means and error bars represent standard error of means. **, $P \le 0.01$; ***, $P \le 0.0001$.

by the blood–brain barrier (57), and heterotopic CH-157MN EV xenografts developed ulceration and necrosis that was not detected with overexpression of NOTCH3^{ICD} (Fig. 3M and N), suggesting NOTCH3 may contribute to meningioma angiogenesis. In support of this hypothesis, immunostaining for endothelial cell markers (CD34 and ERG) was increased in CH-157MN meningioma xenografts with overexpression of NOTCH3^{ICD} compared with EV (Fig. 3O).

NOTCH3 Signaling Drives Meningioma Resistance to Radiotherapy

To determine if NOTCH3 underlies meningioma recurrence after standard interventions, differential expression (Supplementary Table S3) and gene ontology analyses (Fig. 4A) were performed on RNA sequencing data from primary (n = 403) compared with recurrent human meningiomas after treatment with surgery and radiotherapy (n = 99; refs. 8, 10). Recurrent meningiomas were distinguished by gene expression programs controlling DNA metabolism, radiotherapy response, cell signaling, and cell proliferation (Fig. 4A; Supplementary Table S3). Recurrent meningiomas were also enriched for IHC expression of the cell proliferation marker Ki-67, the proportion of deconvolved NOTCH3+ meningioma mural cells from bulk RNA sequencing, and the expression of *NOTCH3* and *HEY1* compared with primary meningiomas (Fig. 4B). These findings were also true if analyses were restricted to primary versus recurrent WHO grade 2 and WHO grade 3 meningiomas. Multiplexed sequential IF (seqIF) on four pairs of patient-matched meningiomas that were treated with radiotherapy between initial and salvage resections showed NOTCH3 and Ki-67 were enriched in recurrent compared with primary tumors (Fig. 4C; Supplementary Table S4). In preclinical models, radiotherapy attenuated the growth of CH-157MN EV xenografts but did not attenuate the growth of CH-157MN NOTCH3^{ICD} xenografts, which had worse survival than CH-157MN EV xenografts despite treatment of both models with ionizing radiation (Fig. 4D).

Single-cell RNA sequencing was performed on CH-157MN xenografts after αNRR3 compared with isotype control treatment (Fig. 3F), or after radiotherapy compared with control treatment with EV or NOTCH3^{ICD} overexpression (Fig. 4D). Xenografts were isolated for single-cell RNA sequencing the day after completing radiotherapy (i.e., early) or once median survival was reached in the control arm (i.e., late) to interrogate early versus late effects of ionizing radiation on meningioma cell types (Fig. 4D). Single-cell transcriptomes were mapped to the human and mouse genomes, revealing 152,464 human meningioma cells and 35,230 mouse microenvironment cells across eight conditions and 23 biological replicates (Supplementary Fig. S12A–S12E). Reduced dimensionality cell clusters were defined using automated cell type classification (25), cell signature gene sets (26), cell cycle analysis (Supplementary Fig. S12B), and differentially expressed cluster marker genes (Supplementary Fig. S13A–S13E; Supplementary Table S5 and S6). Genetic activation (NOTCH3^{ICD}) or pharmacologic inhibition of NOTCH3 with αNRR3 influenced the neutrophil, fibroblast, Langerhans cell, conventional dendritic cell, NK cell, and mural cell composition of meningioma xenografts (Supplementary Fig. S13C–S13E), and NOTCH3+ cells in human meningiomas that were analyzed using multiplexed seqIF expressed multiple regulators of interferon signaling and innate immune responses (STING, pSTAT3; Fig. 4C). Radiotherapy induced early monocyte infiltration (Supplementary Fig. S13C–S13E) and increased interferon and innate immune gene expression from meningioma cells that diminished over time but was conserved across NOTCH3^{ICD} and EV conditions (Fig. 4E and F; Supplementary Fig. S13A and S13B). Cell cycle analysis across single-cell clusters revealed meningioma cell proliferation was increased by NOTCH3^{ICD} and inhibited by αNRR3 (Fig. 4G). Moreover, radiotherapy inhibited meningioma cell cycle progression in EV xenografts, but NOTCH3^{ICD} sustained the cell cycle through the G2M and S phase and increased cell cycle progression in meningioma xenograft samples from late radiotherapy timepoints (Fig. 4H). These data suggest that NOTCH3 drives meningioma resistance to radiotherapy by maintaining cell cycle progression. In support of this hypothesis, radiotherapy in combination with αNRR3 was more effective than radiotherapy alone at blocking the growth and improving survival from CH-157MN xenografts (Fig. 4I).

DISCUSSION

Here, we report that NOTCH3+ cells from the perivascular stem cell niche drive meningioma tumorigenesis and resistance to radiotherapy and find that NOTCH3+ mural cells are conserved across mammalian meningiomas. Our results reveal a new therapeutic vulnerability to treat meningiomas that are resistant to standard interventions, and more broadly suggest that NOTCH3 signaling represents a druggable dependency to treat the most common primary intracranial tumor.

We show that meningioma vasculature is comprised of endothelia from the tumor microenvironment and tumor cells that may fulfill mural cell functions (Fig. 1A–C). Within this milieu, NOTCH3 signaling between meningioma mural cells and endothelia (Fig. 1D) and NOTCH3-mediated intratumor angiogenesis (Fig. 3O) may contribute to meningioma migration into surrounding tissues. Meningiomas without evidence of direct brain parenchyma invasion can nevertheless migrate into perivascular Virchow-Robin spaces that surround perforating arteries and veins in the adjacent brain (Supplementary Fig. S14A–S14C). This unique pattern of cell migration suggests that microscopic positive margins along adjacent brain vasculature may contribute to meningioma recurrence after surgery and radiotherapy and that targeting NOTCH3+ meningioma mural cells or NOTCH3 signaling may improve meningioma outcomes in human patients.

NOTCH3+ meningioma mural cells demonstrate several hallmarks of cancer stem cells (18), such as driving meningeal (Fig. 2G) and meningioma cell proliferation (Figs. 3E, 4G, and H), clonogenic growth (Fig. 3J), tumor-initiating capacity (Fig. 3C and K), angiogenesis (Fig. 3M–O), and resistance to treatment (Fig. 4D and I). NOTCH3 marks cancer stem cells in lung, colon, and breast cancers (31, 58–60), and despite diffuse NOTCH3 expression in meningiomas, only NOTCH3+ meningioma mural cells express other cancer stem cell markers, such as *THY1* (Supplementary Fig. S1G; refs. 32, 33). Considering the histologic (1) and clinical diversity of meningiomas (21–23), it is likely that other stem or progenitor cells may contribute to meningioma tumorigenesis, particularly for Merlin-intact meningiomas, which often encode two wild-type copies of the *NF2* tumor suppressor gene and are enriched at the skull base. If meningiomas from different molecular or histologic groups or from different anatomic compartments arise from different stem or progenitor cells, it is possible that the vascular phenotypes we report may be unique to meningiomas that arise NOTCH3+ meningioma mural cells.

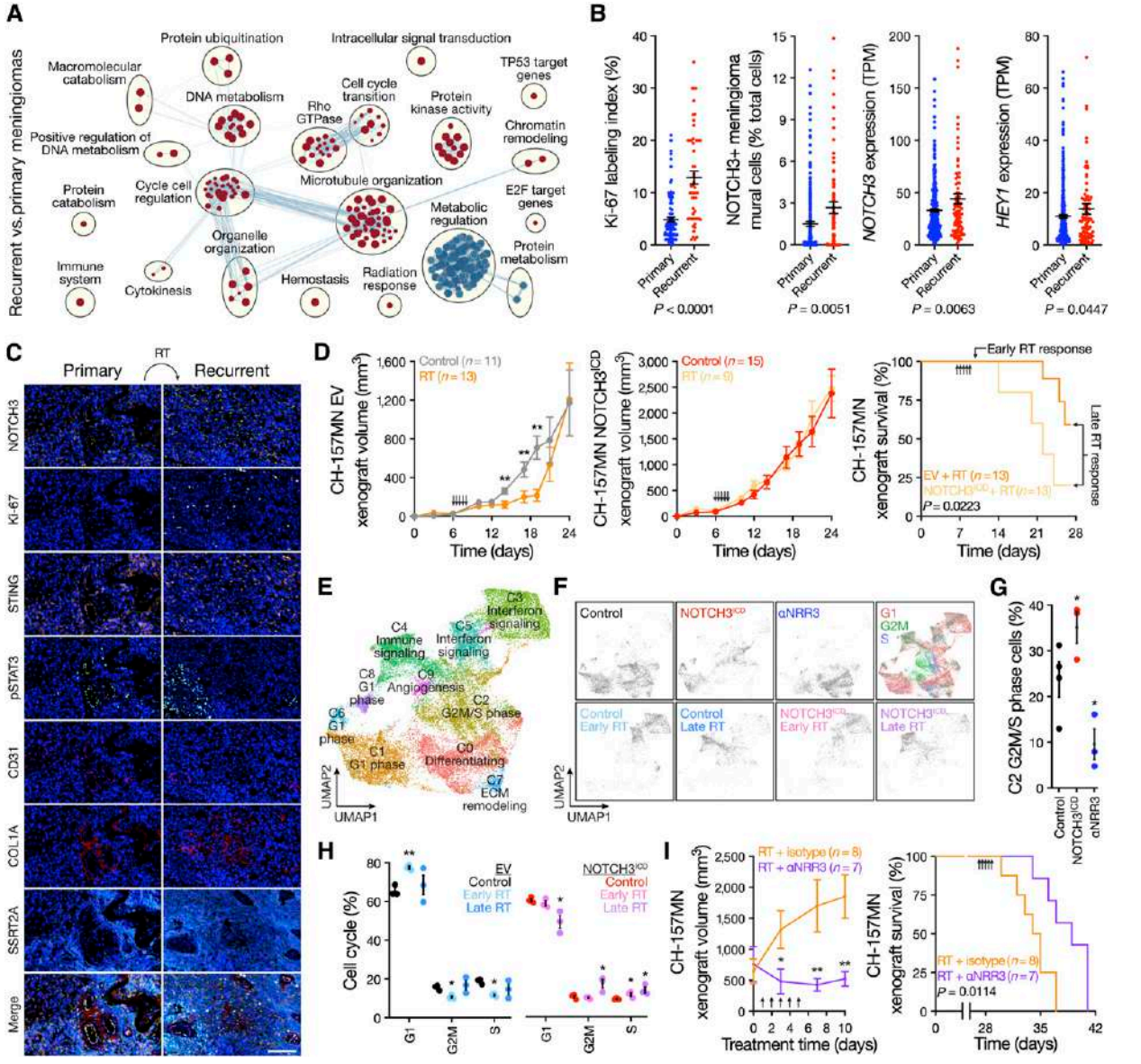

Figure 4. NOTCH3 signaling drives meningioma resistance to radiotherapy. **A,** Network of gene circuits distinguishing recurrent ($n = 99$) from primary ($n = 403$) human meningiomas using RNA sequencing. Nodes represent pathways and edges represent shared genes between pathways ($P \leq 0.01$, FDR ≤ 0.01). Red nodes are enriched and blue nodes are suppressed in recurrent vs. primary meningiomas. **B,** IHC for Ki-67 in recurrent ($n = 53$) vs. primary ($n = 123$) meningiomas, or RNA sequencing of recurrent ($n = 99$) vs. primary ($n = 403$) meningiomas for deconvolution of NOTCH3$^+$ meningioma mural cells from Fig. 1A or quantification of *NOTCH3* or *HEY1* expression. TPM, transcripts per million. ANOVA. **C,** Multiplexed seqIF microscopy showing human meningioma recurrence after radiotherapy (RT) is associated with increased NOTCH3 and Ki-67. Many NOTCH3$^+$ cells also express the interferon and innate immune regulators STING and pSTAT3. CD31 marks pericytes, COL1A marks fibroblasts, SSTR2A marks meningioma cells, and DAPI marks DNA. Representative of $n = 4$ pairs of patient-matched primary and recurrent meningiomas. Scale bar, 100 μm. **D,** CH-157MN meningioma xenograft growth (left and middle, Student's *t*-tests) or survival (log-rank test) after expression of empty vector (EV) or NOTCH3^{ICD} ± RT showing NOTCH3 drives resistance to RT. Arrows indicate RT treatments (2 Gy × 5 daily fractions). Xenografts from all arms were isolated for single-cell RNA sequencing 1 day after completing RT (early) or once median survival was reached in the EV + RT arm (late). **E,** Single-cell RNA sequencing UMAP of 152,464 meningioma xenograft human cell transcriptomes showing tumor cell states ± αNRR3 treatment for 2 weeks as in Fig. 3F or ± NOTCH3^{ICD} ± RT as in **D**. **F,** UMAP showing single-cell RNA sequencing of meningioma xenograft human cells shaded by experimental condition or phase of the cell cycle. **G,** Analysis of C2 G2M/S phase meningioma xenograft human cells in control vs. NOTCH3^{ICD} vs. αNRR3 conditions showing NOTCH3 drives meningioma cell proliferation. Colors as in **F**. Student's *t*-tests. **H,** Cell cycle analysis across all clusters of meningioma xenograft human cells ± NOTCH3^{ICD} ± RT showing NOTCH3 sustains cell proliferation through G2M and S phase despite RT. Student's *t*-test. **I,** Meningioma xenograft growth (left, Student's *t*-tests) or survival (log-rank test) after treatment with RT as in **D** ± αNRR3 as in Fig. 3F. αNRR3 treatment was initiated on the first day of radiotherapy and continued until death. Lines represent means and error bars represent standard error of means. *, $P < 0.05$; **, $P \leq 0.01$.

As more therapies become available for meningiomas, the identification of tumors that may benefit the most from new treatments will be of the utmost importance for designing successful clinical trials. *NOTCH3* and NOTCH3 target genes are enriched in high-grade (Fig. 1I) and recurrent meningiomas (Fig. 4B). Despite enrichment of total *NOTCH3* expression in high-grade meningiomas (Fig. 1I), we found similar proportions of NOTCH3$^+$ meningioma mural cells across WHO grades (ANOVA = 0.0945), suggesting these cells may contribute to meningioma tumorigenesis irrespective of WHO grade. Despite the enrichment of NOTCH3$^+$ meningioma mural cells in immune-enriched meningiomas (Fig. 3A), we found similar proportions of NOTCH3 expression across meningioma DNA methylation groups (ANOVA, $P = 0.1342$), suggesting that meningiomas across all DNA methylation groups may benefit from treatment with αNRR3. An analysis of a subset of recurrent hypermitotic meningiomas using RNAScope showed enrichment in *NOTCH3* expression (Supplementary Fig. S15), suggesting benefit from treatment with αNRR3 may also depend on clinical presentation and prior therapy. Whether the proportion of NOTCH3$^+$ meningioma mural cells or overall NOTCH3 expression in meningiomas will better predict response to αNRR3 is an open question. We speculate that αNRR3 may be of particular benefit for immune-enriched meningiomas and one of several beneficial sequential or combination molecular therapies for hypermitotic meningiomas (with particular benefit for tumors that are recurrent after prior radiotherapy). Clinical trials will be essential for answering these questions, and we hope that our data will provide momentum for such studies in the future.

This study should be interpreted in the context of its limitations, particularly with respect to the preclinical models used for functional interrogation of NOTCH3 signaling in meningiomas. First, our genetically engineered mouse model that integrated *Notch3-Cre^{ERT2}* and *Nf2$^{fl/fl}$* alleles only developed meningeal hyperproliferation (and not overt tumors) after 1 year (Fig. 2G). These data suggest that additional time or additional genetic hits may be required for meningioma tumorigenesis in mice and that future models may wish to incorporate overexpression of additional drivers that are known to be important in aggressive meningiomas in humans, such as FOXM1 (61). Second, the mechanism of NOTCH3 overexpression that we used *in vitro* and in xenografts was a constitutive expression of the activated ICD domain, meaning that our overexpression experiments do not account for counterregulatory mechanisms involving the NRR or γ-secretase complex (but, given the efficacy of αNRR3 in preclinical experiments, this may not be clinically relevant). Third, we studied resistance to radiotherapy using meningioma xenografts grown in the flanks of mice. Although meningiomas grow outside the blood–brain barrier, suggesting similar immune trafficking and bioavailability of drugs compared with the periphery, the reaction of the tumor microenvironment to radiotherapy in the periphery may differ from that in the meningeal space. Thus, studying NOTCH3 in the context of meningioma proliferation, tumor-initiating capacity, and resistance to radiotherapy using skull base xenografts may yield additional insights in the future.

Considering the clinical applications of the findings in this study, the safety and efficacy of selective NOTCH3 inhibition have not been defined in humans, but *Notch3* knockout mice are viable and fertile (62), and we found that diphtheria toxin ablation of NOTCH3$^+$ cells *in utero* or in adulthood using *Notch3-Cre^{ERT2}* and *ROSA^{iDTR}* alleles (63) was not associated with neurologic symptoms or other overt phenotypes. In contrast to αNRR3, αNRR1 did not block the growth of meningioma xenografts (Fig. 3F and 3G) and was associated with significant skin rash and diarrhea leading to weight loss (Supplementary Fig. S16A). We found that a small molecule inhibitor of the γ-secretase complex blocked meningioma xenograft growth, but also caused significant skin rash, diarrhea, and weight loss in mice (Supplementary Fig. S16B and S16C). In sum, these data suggest that αNRR3 may be a safe and effective systemic therapy to treat meningiomas that are resistant to standard interventions in humans.

METHODS

Inclusion and Ethics

This study complied with all relevant ethical regulations and was approved by the UCSF Institutional Review Board (13-12587, 17-22324, 17-23196, and 18-24633). As part of routine clinical practice at UCSF, all human patients who were included in this study signed a written waiver of informed consent to contribute deidentified data to research projects. As part of routine clinical practice at the University of California Davis, all owners of dog meningioma patients who were included in this study signed a written waiver of informed consent to contribute deidentified data to research projects. This study was approved by the UCSF Institutional Animal Care and Use Committee (AN191840), and all experiments complied with relevant ethical regulations.

Single-cell RNA Sequencing

Single cells were isolated from fresh tumor or tumor-adjacent dura samples from human or dog meningiomas, or from meningioma xenografts, as previously described (8). Single-cell suspensions were processed for single-cell RNA sequencing using the Chromium Single Cell 3′ GEM, Library & Gel Bead Kit v3.1 (1000121, 10× Genomics) and a 10× Chromium controller, using the manufacturer-recommended default protocol and settings at a target cell recovery of 5,000 cells per sample. Libraries were sequenced on an Illumina NovaSeq 6000, targeting >50,000 reads per cell, at the UCSF Center for Advanced Technology. Library demultiplexing, read alignment, identification of empty droplets, and UMI quantification were performed using CellRanger (https://github.com/10xGenomics/cellranger). Cells were filtered based on the number of unique genes and single-cell UMI count data were preprocessed in R with the Seurat (64, 65) package (v4.3.0) using the sctransform workflow (66). Dimensionality reduction was performed using principal component (PC) analysis. Uniform manifold approximation and projection (UMAP) and Louvain clustering were performed on the reduction data, followed by marker identification and differential gene expression.

Clusters were defined using a combination of automated cell type classification (25), cell signature gene sets (26), cell cycle analysis, and differentially expressed cluster marker genes. The ScType R package was used for automated cell type classification, with default parameters and package-provided marker genes specific to each cell type (25). Gene set enrichment analysis was performed on clusters using cell type signature gene sets from MSigDB (https://www.gsea-msigdb.org/gsea/msigdb) with the fgsea R package (Bioconductor v3.16). Cell cycle phases of individual cells were assigned with the "CellCycleScoring" function in Seurat, using single-cell cell cycle marker genes (67).

Human meningioma single-cell samples were aligned to the GRCh38 human reference genome; filtered to cells with greater than 250 unique genes, less than 7,500 unique genes, and less than 25% of reads attributed to mitochondrial transcripts; scaled based on regression of UMI count and percentage of reads attributed to mitochondrial genes per cell; and corrected for batch effects using Harmony (24). Parameters for downstream analysis were a minimum distance metric of 0.4 for UMAP, a resolution of 0.2 for Louvain clustering, and a minimum difference in fraction of detection of 0.4 and a minimum log-fold change of 0.5 for marker identification. All human meningiomas analyzed using single-cell RNA sequencing in this study had DNA methylation profiles classifying as immune-enriched or hypermitotic (8) or had biallelic inactivation of *NF2* including loss of at least one copy of chromosome 22q from targeted next-generation DNA sequencing (68).

Dog meningioma single-cell samples were aligned to the ROSCfam1.0 canine reference genome, filtered to cells with greater than 1,000 unique genes and less than 6,500 unique genes, scaled based on regression of UMI count, and corrected for batch effects using Harmony (24). Parameters for downstream analysis were a minimum distance metric of 0.2 for UMAP, a resolution of 0.2 for Louvain clustering, and a minimum difference in fraction of detection of 0.25, and a minimum log-fold change of 0.8 for marker identification.

Meningioma xenograft single-cell samples were aligned to a multi-species reference genome comprised of the GRCh37 human reference genome and the GRCm38 mouse reference genome. Cells were classified as human or mouse cells based on the percentage of UMIs aligning with each genome and the distribution of those percentages. Cells with >97% of UMIs aligning to the human genome were classified as human cells, whereas cells with >75% of UMIs aligning to the mouse genome were classified as mouse cells. Human and mouse cells were analyzed independently after alignment.

Meningioma xenograft human tumor cells were filtered to cells with greater than 200 unique genes, less than 9,000 unique genes, and less than 20% of reads attributed to mitochondrial transcripts; and scaled based on regression of UMI count and percentage of reads attributed to mitochondrial genes per cell. Parameters for downstream analysis were a minimum distance metric of 0.1 for UMAP, a resolution of 0.2 for Louvain clustering, and a minimum difference in fraction of detection of 0.3 and a minimum log-fold change of 0.25 for marker identification.

Meningioma xenograft mouse microenvironment cells were filtered to cells with greater than 250 unique genes, less than 7,500 unique genes, and less than 5% of reads attributed to mitochondrial transcripts and scaled based on regression of UMI count and percentage of reads attributed to mitochondrial genes per cell. Parameters for downstream analysis were a minimum distance metric of 0.2 for UMAP, a resolution of 0.2 for Louvain clustering, and a minimum difference in fraction of detection of 0.5 and a minimum log-fold change of 0.5 for marker identification.

Single-cell RNA Sequencing Analysis

Single human meningioma cells were classified as tumor or non-tumor cells based on copy number loss of chromosome 22q. All human meningiomas analyzed using single-cell RNA sequencing in this study had copy number loss of chromosome 22q from DNA methylation profiling or targeted next-generation DNA sequencing (68). The presence or absence of copy number variants in individual cells was assessed using the CONICSmat R package (v1.0; ref. 27). Briefly, a two-component Gaussian mixture model was fit to the average expression values of genes on chromosome 22q across all cells assessed. The command "plotAll" from CONICSmat was run with the parameters "repetitions = 100, postProb = 0.8." Cells with a posterior probability less than 0.2 were identified as tumors, whereas cells with a posterior probability greater than 0.8 were identified as normal.

The cell–cell communication network for the Notch signaling pathway was inferred and visualized using the CellChat R package (v1.5.0; ref. 34). Briefly, differentially expressed signaling genes were identified, noise was mitigated by calculating the ensemble average expression, intercellular communication probability was calculated by modeling ligand-receptor interactions using the law of mass action, and statistically significant communications were identified. The command "computeCommunProb" from CellChat was run with the parameters "raw.use = FALSE, nboot = 20." All other commands were run with default parameters.

Human meningioma single-cell cluster identities were projected onto reduced dimensionality clusters of dog meningioma cells using the commands "FindTransferAnchors" and "TransferData" from Seurat. The parameter "normalization.method = 'SCT'" was used for "FindTransferAnchors" and defaults were used for all other parameters for both commands.

Bulk RNA Sequencing Analysis

Human meningioma bulk RNA sequencing data were generated and analyzed as previously described (8, 10). In brief, RNA was extracted from frozen meningiomas, and library preparation was performed using the TruSeq Standard mRNA Kit (20020595, Illumina) 50-bp single-end or 150-bp paired-end reads that were sequenced on an Illumina NovaSeq 6000 to a mean of 20 million reads per sample. Analysis was performed using a pipeline comprised of FastQC for quality control, and Kallisto for reading pseudoalignment and transcript abundance quantification using the default settings (v0.46.2).

Gene set enrichment analysis (v4.3.2) was performed to identify differentially expressed pathways distinguishing recurrent from primary meningiomas. Gene rank scores were calculated using the formula sign($\log_2$ fold-change) × −log10(*P*-value). Pathways were defined using the gene set file Human_GOBP_AllPathways_no_GO_iea_December_01_2022_symbol.gmt, which is maintained by the Bader laboratory. Gene set size was limited to range between 15 and 500, and positive and negative enrichment files were generated using 2000 permutations. The EnrichmentMap App (v3.3.4) in Cytoscape (v3.7.2) was used to visualize the results of pathway analysis. Nodes with $P \leq 0.01$ and FDR ≤ 0.01, and nodes sharing gene overlaps with Jaccard + Overlap Combined threshold of 0.375 were connected by blue lines (edges) to generate network maps. Clusters of related pathways were identified and annotated using the AutoAnnotate app (v1.3.5) in Cytoscape, which uses a Markov cluster algorithm to connect pathways by shared keywords in the description of each pathway. The resulting groups of pathways were designated as the consensus pathways in each circle.

Histology, IHC, IF, and Microscopy

For adult human tissue samples, deparaffinization and rehydration of 5-μm formalin-fixed, paraffin-embedded (FFPE) tissue sections and hematoxylin and eosin (H&E) staining were performed using standard procedures. Immunostaining was performed on an automated Ventana Discovery Ultra staining system and detection was performed with Multimer HRP (Ventana Medical Systems) followed by fluorescent detection (DISCOVERY Rhodamine and CY5) or DAB. Immunostaining for NOTCH3 was performed using mouse monoclonal NOTCH3/N3ECD primary antibody (MABC594, Millipore Sigma, 1:25–1:100) with incubation for 32 min following CC1 antigen retrieval for 32 min. For dual staining, primary antibody incubations were carried out serially with the inclusion of positive, negative, and single antibody controls. Following staining for NOTCH3/N3ECD, tissue sections were stained with primary antibodies recognizing CD34 (CBL496, Millipore Sigma, mouse monoclonal, 1:300) for 2 h, SMA (ab7817, Abcam, mouse polyclonal, 1:30,000) for 32 min, or VWF (A0082, Dako, rabbit polyclonal, 1:1,000) for 20 min. All IF experiments were imaged on an LSM 800 confocal laser scanning microscope

with Airyscan (Zeiss) and analyzed using ImageJ. Intensity and extent of NOTCH3 immunoreactivity adjacent to blood vessels or within cellular tumors were scored on a semi-quantitate basis by a board-certified neuropathologist who was blinded to WHO grade. Intensity was scored as 1 = minimal/weak, 2 = moderate, or 3 = strong, whereas extent was scored as 1 = absent/focal, 2 = patchy (less than ~50% examined area), or 3 = extensive (greater than ~50% examined area). The total score was calculated as a product of intensity and extent scores for each compartment (blood vessels vs. cellular tumor) for each case and compared across WHO grades.

For meningioma xenograft samples, deparaffinization and rehydration of 5-μm FFPE tissue sections and H&E staining were performed using standard procedures. IHC was performed on an automated Ventana Discovery Ultra staining system using primary antibodies recognizing Ki-67 (M7240, DAKO, mouse monoclonal, clone MIB1, 1:50) for 30 min, CD34 (NCL-L-END, LEICA, mouse monoclonal, clone QBEnd/10, undiluted) for 15 min, or ERG (790-4576, Ventana, rabbit monoclonal, clone EPR3864, undiluted) for 32 min. All histologic and IHC experiments were imaged on a BX43 light microscope (Olympus) and analyzed using the Olympus cellSens Standard Imaging Software package.

For IF of the developing human brain, de-identified tissue samples were collected with previous patient consent in strict observance of legal and institutional ethical regulations. Autopsy consent and all protocols were approved by the UCSF Human Gamete, Embryo, and Stem Cell Research Committee. All cases were determined by chromosomal analysis, physical examination, and/or pathologic analysis to be control tissues, which indicates that they were absent of neurologic disease. Brains were cut into ~1.5cm coronal or sagittal blocks, fixed in 4% paraformaldehyde for 2 days, and then cryoprotected in a 30% sucrose solution. Blocks were cut into 30 μm sections on a cryostat, mounted on glass slides for IF, and stored at −80°C. Frozen slides were moved from −80°C to 4°C the night prior to staining and then to the lab bench for 2 h before beginning the immunostaining protocol. Slides were washed once with 1X PBS for 5 min, then once with 1X TBS for 5 min before blocking with TBS++++ (goat serum, BSA, albumin, glycine, and triton X in TBS) for 1 h. Primary antibodies recognizing PDGFRB (AF385, R&D Systems, 1:200), CD34 (AF7227, R&D Systems, 1:200), or NOTCH3/N3ECD as described above were used with overnight incubation at room temperature at 1:200 dilutions in TBS++++. The following day, three 1× TBS washes were performed before incubating with secondary antibodies in TBS++++ for 2 h. After three additional TBS washes, DAPI (4′,6-diamidino-2-phenylindole, 62248, Thermo Fisher Scientific) was added, and the slides were mounted.

IF of meningioma cell lines were performed on cover glass slips in culture. Cells were fixed in 4% PFA in PBS for 8 min, washed in PBS, and blocked for 30 min in 5% donkey serum and 0.1% Triton-X100 in PBS. Cells were stained with PTPRZ1 (sc-33664, Santa Cruz Biotechnology, 1:1,000) overnight at 4°C and subsequently labeled with rabbit Alexa Fluor secondary antibody (A21206, Thermo Fisher Scientific, 1:1,000) and Hoechst 33342 to mark DNA for 1 h at room temperature prior to mounting and imaging. Meningioma cells were imaged on an LSM 800 confocal laser scanning microscope with Airyscan (Zeiss) and analyzed using ImageJ.

RNAScope and Microscopy

The RNAScope Multiplex Fluorescent V2 assay (32310, ACDBio) was performed according to the manufacturer's protocol. Briefly, 5-μm FFPE meningioma sections were incubated with hydrogen peroxide to inhibit endogenous peroxidase, followed by processing for target retrieval and treatment with ProteasePlus. Meningioma sections were subsequently incubated with RNA probes for *NOTCH3* (558991-C2, Hs-NOTCH3-C2) and *NF2* (1037481-C, Hs-NF2-C1), followed by revelation and amplification steps. Meningioma sections were blocked (5% normal donkey serum, 1X Animal Free blocking, 0.3% Triton X-100) for 1 h at room temperature and incubated with primary antibody against VE-cadherin (AF938, R&D Systems, 1:100) overnight at 4°C. The next day, meningioma sections were incubated with secondary antibodies for 1 h at room temperature and counterstained with DAPI (62248, Thermo Fisher Scientific). Meningioma sections were imaged on an LSM 800 confocal laser scanning microscope with Airyscan (Zeiss) and analyzed using ImageJ.

Multiplexed Sequential IF and Microscopy

Automated multiplexed sequential immunofluorescence (seqIF) staining and imaging were performed on FFPE sections at Northwestern University using the COMET platform (Lunaphore Technologies). The multiplexed panel was comprised of 29 antibodies (Supplementary Table S4). The 29-plex protocol was generated using the COMET Control Software, and reagents were loaded onto the COMET device to perform seqIF. All antibodies were validated using conventional IHC and/or IF staining in conjunction with corresponding fluorophores and DAPI (62248, Thermo Fisher Scientific). For optimal concentration and the best signal-to-noise ratio, all antibodies were tested at three different dilutions: starting with the manufacturer-recommended dilution (MRD), MRD/2, and MRD/4. Secondary Alexa fluorophore 555 (A32727, Thermo Fisher Scientific) and Alexa fluorophore 647 (A32733, Thermo Fisher Scientific) were used at 1:200 or 1:400 dilutions, respectively. The optimizations and full runs of the multiplexed panel were executed using the seqIF technology integrated into the Lunaphore COMET platform (characterization 2 and 3 protocols, and seqIF protocols, respectively). The seqIF workflow was parallelized on a maximum of four slides, with automated cycles of iterative staining of two antibodies at a time, followed by imaging, and elution of the primary and secondary antibodies, with no sample manipulation during the entire workflow. All reagents were diluted in a Multistaining Buffer (BU06, Lunaphore Technologies). The elution step lasted 2 min for each cycle and was performed with Elution Buffer (BU07-L, Lunaphore Technologies) at 37°C. Quenching lasted for 30 s and was performed with Quenching Buffer (BU08-L, Lunaphore Technologies). Incubation time was set at 4 min for all primary antibodies, except for the p16 antibody at 8 min, and secondary antibodies at 2 min. Imaging was performed with Imaging Buffer (BU09, Lunaphore Technologies) with exposure times set for 400 ms for the TRITC (tetramethylrhodamine) channel, 200 ms for the Cy5 channel, and 80 ms for the DAPI channel. Imaging was performed with Imaging Buffer (BU09, Lunaphore Technologies) with exposure times set at 4 min for all primary antibodies, except P16 antibody at 8 min, and secondary antibodies at 2 min. Imaging was performed with an integrated epifluorescent microscope at 20× magnification. Image registration was performed immediately after concluding the staining and imaging procedures by COMET Control Software. Each seqIF protocol resulted in a multi-stack OME-TIFF file in which the imaging outputs from each cycle were stitched and aligned. COMET OME-TIFF files contain a DAPI image, intrinsic tissue autofluorescence in TRITC and Cy5 channels, and a single fluorescent layer per marker. Markers were subsequently pseudocolored for visualization of multiplexed antibodies.

Mouse Genetic Models

Notch3$^{tm1.1(cre/ERT2)Sat}$ (*Notch3-Cre*^{ERT2}) mice were obtained from the Sweet-Cordero Lab at UCSF. Ptgds$^{tm1.1(cre)Gvn}$ (*Ptgds-Cre*) mice were obtained from Riken. Gt(ROSA)26Sor$^{tm4(ACTB-tdTomato,-EGFP)Luo}$ (*ROSA*$^{mT/mG}$) mice were obtained from The Jackson Laboratory. Gt(ROSA)26Sor$^{tm1(HBEGF)Awai/J}$ (*ROSA*^{iDTR}) mice were obtained from The Jackson Laboratory. FVB.129P2-Nf2^{tm2Gth} (*Nf2*$^{fl/fl}$) mice were obtained from Riken. All mouse genetic experiments were performed on the C57BL/6J background. Mice were intercrossed to generate *Notch3-Cre*$^{ERT2(+/WT)}$ *ROSA*$^{mT/mG}$ mice, *Ptgds-Cre*$^{+/WT}$ *ROSA*$^{mT/mG}$ mice, *Notch3-Cre*$^{ERT2(+/WT)}$ *Nf2*$^{fl/fl}$ mice, and *Notch3-Cre*$^{ERT2(+/WT)}$ *ROSA*^{iDTR}

mice. Recombination of either the *Nf2* or *ROSA* locus was induced using intraperitoneal injection of 75 mg/kg of tamoxifen (T5648, Sigma–Aldrich) dissolved in corn oil. For *in utero* recombination, pregnant dams were injected with tamoxifen once at E16.5 and their subsequent litters were genotyped and euthanized at the indicated timepoints. For postnatal recombination, mice were injected daily five times with tamoxifen and euthanized at the indicated timepoints.

Mouse skullcaps were used for meningeal lineage tracing experiments and intact skulls were used to assess for meningeal hyperproliferation. In brief, mice were perfused with 4°C 4% paraformaldehyde in 80-nmol/L PIPES (piperazine-*N*,*N*′-bis(2-ethanesulfonic acid)), pH 6.8, 5-mmol/L EGTA (egtazic acid), and 2-mmol/L $MgCl_2$. Muscle was dissected and removed, and samples were rotated overnight at 4°C in perfusion solution. Samples were washed three times for 5 min in PBS and decalcified for 3 days rotating at 4°C in 20% EDTA (ethylenediaminetetraacetic acid), pH 7.4, in PBS. For meningioma tumorigenesis experiments, whole skulls were subsequently embedded in 5% low-melt agarose (Precisionary) and cut into 300-µm sections on a Vibratome (VT1000S, Leica). Sections were stained for 15 s in Mayer's hematoxylin solution (MHS16, Sigma–Aldrich), washed three times for 5 min in distilled water, incubated for 1 min in PBS to blue nuclei, washed for 5 min in distilled water, stained for 30 s in 0.5% Eosin Y (1099884, Sigma–Aldrich), washed two times for 5 min in 70% ethanol, and mounted on slides using Vectashield Antifade Mounting Media (H-1000-10, Vector Laboratories).

Mouse Xenograft Models and Treatments

Xenograft experiments were performed by implanting CH-157MN or IOMM-Lee cells into the flank of 5- to 6-week-old female NU/NU mice (Harlan Sprague Dawley) as previously described (8). Tumor-initiating capacity was defined by the development of sustained, iteratively increasing subcutaneous growth at injection sites. Radiotherapy treatments were performed using a Precision X-RAD 320 Cabinet Irradiator with normal operating settings to deliver 2Gy of ionizing radiation on each of five consecutive days. NOTCH3 negative regulatory region neutralizing antibody treatments (αNRR3) and NOTCH1 negative regulatory region neutralizing antibody (αNRR1) treatments using murine antibodies from Genentech were performed as previously described (54, 55), with biweekly IP injection of 20-mg/kg αNRR3, 10-mg/kg αNRR1 (dose-reduced due to gastrointestinal and cutaneous toxicity leading to weight loss), or 20-mg/kg IgG2a isotype control (BE0085, Bio X-cell). γ-Secretase inhibitor treatments were performed using LY-411575 (SML0649, Millipore Sigma) as previously described (46), with daily 20-µmol/L/kg IP injections in 0.5% methylcellulose and 0.1% Tween 80 in 1X PBS. For Kaplan–Meier survival analyses, events were recorded when tumors reached the protocol-defined size of 2,000 mm^3, mice developed mobility or physiologic impairment from tumor burden, or mice lost >15% of body weight due to treatment-associated toxicity.

Cell Culture

HEK293T cells (CRL-3216, ATCC), IOMM-Lee (52) meningioma cells (CRL-3370, ATCC), and CH157-MN (51) and BenMen (53) meningioma cells (which were obtained from collaborators) were cultured in DMEM (11960069, Life Technologies) supplemented with 10% FBS, 1× GlutaMAX (35050-061, Thermo Fisher Scientific) and 1× penicillin/streptomycin (15140122, Life Technologies). Cell lines were confirmed to be mycoplasma-free at regular internals and were validated using SSTR profiling and DNA methylation profiling.

To generate cell lines overexpressing NOTCH3 ICD, pLVX-Puro plasmid containing pCMV6-NOTCH3ICD was generated. Lentiviral particles were produced by transfecting HEK293T cells with standard packaging vectors using the *Trans*IT-Lenti Transfection Reagent (6605, Mirus). CH157-MN cells were stably transduced with lentiviral particles to generate CH-157MN $NOTCH3^{ICD}$ or empty pLVX vector (EV) cells. Successfully transduced cells were isolated using Puromycin selection, and NOTCH3 overexpression was confirmed using QPCR.

For clonogenic assays, 250 cells were seeded in triplicate for each condition in a 6-well plate and grown for 10 days in standard culture media. Cells were fixed in methanol for 30 min, washed and stained in 0.01% crystal violet (C6158, Sigma–Aldrich) for 3 h, washed three times in distilled water, and dried overnight. Cells were imaged on a Stemi 508 stereo microscope (Zeiss) and the clonogenic area was quantified in ImageJ.

Immunoblotting

Meningioma cells for immunoblotting were lysed in 1% SDS in 100-mmol/L pH 6.8 Tris-HCL containing protease and phosphatase inhibitor (A32961, Thermo Scientific), vortexed at maximum speed for 1 min, rocked at 4°C for 5 min, and centrifuged at 4°C for 15 min at 15,000 × *g*. Supernatant protein quantification was performed using BCA assays (23225, Pierce); 20 µg of lysate from each cell line was boiled for 15 min in Laemmli reducing buffer. Proteins were separated on 4%–15% TGX precast gels (5671084, Bio-Rad), and transferred onto ImmunBlot PVDF membrane (1620177, Bio-Rad). Membranes were blocked in 5% milk in TBST (tris-buffered saline, .1% Tween-20), incubated in primary antibodies, washed, and incubated in secondary antibodies. Membranes were subjected to immunoblot analysis using Pierce ECL substrate (32209, Thermo Fischer Scientific). Primary antibodies recognizing NOTCH3 (5276, Cell Signaling, 1:1,000) or GAPDH (8245, Abcam, 1:5,000) and secondary antibodies recognizing mouse (7076, Cell Signaling, 1:2,000) or rabbit (7074, Cell Signaling, 1:2,000) epitope were used.

Quantitative Reverse-Transcriptase Polymerase Chain Reaction

RNA was extracted from cultured meningioma cells using the RNeasy Mini Kit (74106, QIAGEN) according to the manufacturer's instructions. cDNA was synthesized from extracted RNA using the iScript cDNA Synthesis Kit (1708891, Bio-Rad). Real-time QPCR was performed using PowerUp SYBR Green Master Mix (A25918, Thermo Fisher Scientific) on a QuantStudio 6 Flex Real-Time PCR system (Life Technologies) using forward and reverse primers (*NOTCH3-F* CGTGGCTTCTTTCTACTGTGC, *NOTCH3-R* CGTTCA CCGGATTTGTGTCAC, *HEY1-F* GTTCGGCTCTAGGTTCCATGT, *HEY1-R* CGTCGGCGCTTCTCAATTATT, *GAPDH-F* GTCTCCTC TGACTTCAACAGCG, and *GAPDH-R* ACCACCCTGTTGCTGTA GCCAA). QPCR data were analyzed using the $^{\Delta\Delta}$Ct method relative to *GAPDH* expression.

Statistics

All experiments were performed with independent biological replicates and repeated, and statistics were derived from biological replicates. Biological replicates are indicated in each figure panel or figure legend. No statistical methods were used to predetermine sample sizes, but sample sizes in this study are similar or larger to those reported in previous publications. Data distribution was assumed to be normal, but this was not formally tested. Investigators were blinded to conditions during clinical data collection and analysis of mechanistic or functional studies. Bioinformatic analyses were performed blind to clinical features, outcomes, or molecular characteristics. The clinical samples used in this study were retrospective and nonrandomized with no intervention, and all samples were interrogated equally. Thus, controlling for covariates among clinical samples was not relevant. Cells and animals were randomized to experimental conditions. No clinical, molecular, or cellular data points were excluded from the analyses. Lines represent means, and error bars represent the standard error of the means. Results were compared using Student's *t*-tests and

ANOVA, which are indicated in figure panels or figure legends alongside approaches used to adjust for multiple comparisons. In general, statistical significance is shown using asterisks (*, $P \leq 0.05$; **, $P \leq 0.01$; ***, $P \leq 0.0001$), but exact *P*-values are provided in figure panels or figure legends when possible.

Data Availability

Single-cell RNA sequencing data of new samples ($n = 1$ human meningioma sample, $n = 3$ canine meningioma samples, $n = 2$ canine dura samples, $n = 23$ meningioma xenograft samples) that are reported in this manuscript are available under the accession GSE235998 (https://www.ncbi.nlm.nih.gov/geo/query/acc.cgi?acc=GSE235998). Additional single-cell RNA sequencing data from previously reported human meningiomas ($n = 4$ meningioma samples, $n = 1$ dura sample) are available under the accession GSE183655 (https://www.ncbi.nlm.nih.gov/geo/query/acc.cgi?acc=GSE183655). RNA sequencing and DNA methylation profiling data of human meningioma samples ($n = 502$) are available under the accessions GSE183656 (https://www.ncbi.nlm.nih.gov/geo/query/acc.cgi?acc=GSE183656), GSE212666 (https://www.ncbi.nlm.nih.gov/geo/query/acc.cgi?acc=GSE212666), GSE183653 (https://www.ncbi.nlm.nih.gov/geo/query/acc.cgi?acc=GSE183653), and GSE101638 (https://www.ncbi.nlm.nih.gov/geo/query/acc.cgi). The publicly available GRCh38 (hg38, https://www.ncbi.nlm.nih.gov/assembly/GCF_000001405.39/), GRCh37 (hg19, https://www.ncbi.nlm.nih.gov/assembly/GCF_000001405.25/), GRCm38 (mm10, https://www.ncbi.nlm.nih.gov/assembly/GCF_000001635.20/), and ROS_Cfam_1.0 datasets (https://www.ncbi.nlm.nih.gov/assembly/GCF_014441545.1/) were used in this study. Source data are provided in this manuscript.

Code Availability

The open-source software, tools, and packages used for data analysis in this study, as well as the version of each program, were ImageJ (v2.1.0), CellRanger (v6.1.2 and v7.1.0), kallisto (v0.46.2), gene set enrichment analysis (v4.3.2), EnrichmentMap (v3.3.4), Cytoscape (v3.7.2), AutoAnnotate (v1.3.5), R (v4.2.3), Seurat R package (v4.3.0), Harmony R package (v0.1.1), ScType R package (v1), CONICSmat R package (v1.0), CellChat R package (v1.5.0), fgsea (Bioconductor v3.16), and DESeq2 (Bioconductor v3.16). No software was used for data collection. No custom algorithms or code were used.

Authors' Disclosures

S.L. Hervey-Jumper reports other support from Gilmartin Capital outside the submitted work. A. Ashworth reports personal fees from Tango Therapeutics, Azkarra, Ovibio, Kyttaro, Cytomx, Cambridge Science Corporation, Genentech, Gladiator, Circle, Bluestar/Clearnote Health, Earli, Ambagon, Phoenix Molecular Designs, Yingli/280Bio, Trial Library, ProLynx, Oric, HapTen, NextRNA, Novartis, and Deciphera outside the submitted work; in addition, A. Ashworth has a patent for the use of NOTCH3 antibodies to treat meningioma pending and hold patents on the use of PARP inhibitors held jointly with AstraZeneca from which he has benefited financially (and may do so in the future). E.E. Crouch reports non-financial support from CellSonics outside the submitted work. No disclosures were reported by the other authors.

Authors' Contributions

A. Choudhury: Conceptualization, resources, data curation, software, formal analysis, validation, investigation, visualization, methodology, writing–original draft, writing–review and editing. M.A. Cady: Formal analysis, validation, investigation, visualization, methodology, writing–original draft, writing–review and editing. C.-H.G. Lucas: Resources, formal analysis, validation, investigation, visualization, writing–review and editing. H. Najem: Resources, formal analysis, validation, investigation, visualization, methodology, writing–review and editing. J.J. Phillips: Formal analysis, validation, investigation, visualization, writing–review and editing. B. Palikuqi: Resources, formal analysis, investigation, visualization, writing–review and editing. N. Zakimi: Data curation, software, formal analysis, investigation, visualization, writing–review and editing. T. Joseph: Formal analysis, writing–review and editing. J.O. Birrueta: Formal analysis, writing–review and editing. W.C. Chen: Formal analysis. N.A. Oberheim Bush: Resources, supervision, writing–review and editing. S.L. Hervey-Jumper: Resources, supervision, writing–review and editing. O.D. Klein: Resources, formal analysis, supervision, visualization, writing–review and editing. C.M. Toedebusch: Resources, formal analysis, supervision, visualization, writing–review and editing. C.M. Horbinski: Resources, formal analysis, visualization, writing–review and editing. S.T. Magill: Resources, software, formal analysis, writing–review and editing. A. Bhaduri: Resources, software, formal analysis, supervision, writing–review and editing. A. Perry: Resources, software, formal analysis, supervision, writing–review and editing. P.J. Dickinson: Resources, formal analysis, supervision, funding acquisition, visualization, writing–review and editing. A.B. Heimberger: Resources, formal analysis, supervision, funding acquisition, visualization, project administration, writing–review and editing. A. Ashworth: Resources, data curation, formal analysis, supervision, funding acquisition, visualization, project administration, writing–review and editing. E.E. Crouch: Conceptualization, resources, data curation, formal analysis, supervision, funding acquisition, validation, investigation, visualization, methodology, writing–original draft, project administration, writing–review and editing. D.R. Raleigh: Conceptualization, resources, data curation, formal analysis, supervision, funding acquisition, validation, investigation, visualization, methodology, writing–original draft, project administration, writing–review and editing.

Acknowledgments

The authors thank Mark Youngblood, Julie Siegenthaler, Sten Linnarsson, Elin Vinsland, Chris Siebel, Fred De Sauvage, Alejandro Sweet-Cordero, Kieren Marini, Kyla Foster, and members of the Raleigh lab for reagents, guidance, and edits, Beverly Sturges and Chai Fei Li for providing dog meningioma samples, Shai and the staff of the UCSF Brain Tumor Center Biorepository and Pathology Core, Eric Chow and the staff of the UCSF Center for Advanced Technology, and Ken Probst and Noel Sirivansanti for Illustrations. Lunaphore COMET multiplexed seqIF was enabled by a gift from the Stephen M. Coffman trust to the Northwestern University Malnati Brain Tumor Institute of the Lurie Cancer Center. This study was supported by the UCSF Wolfe Meningioma Program Project and the National Institutes of Health (NIH) grants F30 CA246808 and T32 GM007618 to A. Choudhury; NIH grants T32 CA15102 and P50 CA097257 to C.-H.G. Lucas; NIH grant P50 CA097257 to J.J. Phillips; NIH grant P50 CA097257 to W.C. Chen; the UCSF Wolfe Meningioma Program Project and P50 CA097257 to N.A. Oberheim Bush; NIH grants R01 NS117104, R01 NS118039, and P50 CA221747 to C.M. Horbinski; the UCSF Wolfe Meningioma Program Project, NIH grant F32 CA213944, and the Northwestern Medicine Malnati Brain Institute of the Lurie Cancer Center to S.T. Magill; NIH grants R01 CA120813, R01 NS120547, and P50 CA221747 to A.B. Heimberger; and NIH grants R01 CA262311 and P50 CA097257, and the Trenchard Family Charitable Fund to D.R. Raleigh.

Note

Supplementary data for this article are available at Cancer Discovery Online (http://cancerdiscovery.aacrjournals.org/).

Received December 4, 2023; revised February 29, 2024; accepted May 10, 2024; published first May 10, 2024.

REFERENCES

1. Louis DN, Perry A, Wesseling P, Brat DJ, Cree IA, Figarella-Branger D, et al. The 2021 WHO classification of tumors of the central nervous system: a summary. Neuro Oncol 2021;23:1231–51.
2. Ostrom QT, Price M, Neff C, Cioffi G, Waite KA, Kruchko C, et al. CBTRUS statistical report: primary brain and other central nervous system tumors diagnosed in the United States in 2015–2019. Neuro Oncol 2022;24(Suppl 5):v1–95.
3. Goldbrunner R, Stavrinou P, Jenkinson MD, Sahm F, Mawrin C, Weber DC, et al. EANO guideline on the diagnosis and management of meningiomas. Neuro Oncol 2021;23:1821–34.
4. Lin D-D, Lin J-L, Deng X-Y, Li W, Li D-D, Yin B, et al. Trends in intracranial meningioma incidence in the United States, 2004–2015. Cancer Med 2019;8:6458–67.
5. Simpson D. The recurrence of intracranial meningiomas after surgical treatment. J Neurosurg 1957;58:51–6.
6. Brastianos PK, Galanis E, Butowski N, Chan JW, Dunn IF, Goldbrunner R, et al. Advances in multidisciplinary therapy for meningiomas. Neuro Oncol 2019;21(Suppl 5):i18–31.
7. Wen PY, Quant E, Drappatz J, Beroukhim R, Norden AD. Medical therapies for meningiomas. J Neurooncol 2010;99:365–78.
8. Choudhury A, Magill ST, Eaton CD, Prager BC, Chen WC, Cady MA, et al. Meningioma DNA methylation groups identify biological drivers and therapeutic vulnerabilities. Nat Genet 2022;54:649–59.
9. Driver J, Hoffman SE, Tavakol S, Woodward E, Maury EA, Bhave V, et al. A molecularly integrated grade for meningioma. Neuro Oncol 2022;24:796–808.
10. Choudhury A, Chen WC, Lucas C-HG, Bayley JC, Harmanci AS, Maas SLN, et al. Hypermitotic meningiomas harbor DNA methylation subgroups with distinct biological and clinical features. Neuro Oncol 2023;25:520–30.
11. Maas SLN, Stichel D, Hielscher T, Sievers P, Berghoff AS, Schrimpf D, et al. Integrated molecular-morphologic meningioma classification: a multicenter retrospective analysis, retrospectively and prospectively validated. J Clin Oncol 2021;39:3839–52.
12. Sahm F, Schrimpf D, Stichel D, Jones DTW, Hielscher T, Schefzyk S, et al. DNA methylation-based classification and grading system for meningioma: a multicentre, retrospective analysis. Lancet Oncol 2017;18:682–94.
13. Patel AJ, Wan Y-W, Al-Ouran R, Revelli J-P, Cardenas MF, Oneissi M, et al. Molecular profiling predicts meningioma recurrence and reveals loss of DREAM complex repression in aggressive tumors. Proc Natl Acad Sci U S A 2019;116:21715–26.
14. Nassiri F, Liu J, Patil V, Mamatjan Y, Wang JZ, Hugh-White R, et al. A clinically applicable integrative molecular classification of meningiomas. Nature 2021;597:119–25.
15. Youngblood MW, Duran D, Montejo JD, Li C, Omay SB, Özduman K, et al. Correlations between genomic subgroup and clinical features in a cohort of more than 3000 meningiomas. J Neurosurg 2019;133:1345–54.
16. Chen WC, Choudhury A, Youngblood MW, Polley M-YC, Lucas C-HG, Mirchia K, et al. Targeted gene expression profiling predicts meningioma outcomes and radiotherapy responses. Nat Med 2023;29:3067–76.
17. Raleigh DR, Preusser M. A 34-gene expression biomarker predicts meningioma outcomes and radiotherapy responses. Neuro Oncol 2024;26:207–8.
18. Hanahan D. Hallmarks of cancer: new dimensions. Cancer Discov 2022;12:31–46.
19. Tohma Y, Yamashima T, Yamashita J. Immunohistochemical localization of cell adhesion molecule epithelial cadherin in human arachnoid villi and meningiomas. Cancer Res 1992;52:1981–7.
20. Yamashima T, Kida S, Yamamoto S. Ultrastructural comparison of arachnoid villi and meningiomas in man. Mod Pathol 1988;1:224–34.
21. Incarbone M, Ceresoli GL, Di Tommaso L, Cappuzzo F, Inzirillo F, Infante M, et al. Primary pulmonary meningioma: report of a case and review of the literature. Lung Cancer 2008;62:401–7.
22. Jadik S, Stan AC, Dietrich U, Pietilä TA, Elsharkawy AE. Intraparenchymal meningioma mimicking cavernous malformation: a case report and review of the literature. J Med Case Rep 2014;8:467.
23. Nakamura M, Roser F, Bundschuh O, Vorkapic P, Samii M. Intraventricular meningiomas: a review of 16 cases with reference to the literature. Surg Neurol 2003;59:490–503.
24. Korsunsky I, Millard N, Fan J, Slowikowski K, Zhang F, Wei K, et al. Fast, sensitive and accurate integration of single-cell data with Harmony. Nat Methods 2019;16:1289–96.
25. Ianevski A, Giri AK, Aittokallio T. Fully-automated and ultra-fast cell-type identification using specific marker combinations from single-cell transcriptomic data. Nat Commun 2022;13:1246.
26. Subramanian A, Tamayo P, Mootha VK, Mukherjee S, Ebert BL, Gillette MA, et al. Gene set enrichment analysis: a knowledge-based approach for interpreting genome-wide expression profiles. Proc Natl Acad Sci U S A 2005;102:15545–50.
27. Müller S, Cho A, Liu SJ, Lim DA, Diaz A. CONICS integrates scRNA-seq with DNA sequencing to map gene expression to tumor sub-clones. Bioinformatics 2018;34:3217–9.
28. Crouch EE, Bhaduri A, Andrews MG, Cebrian-Silla A, Diafos LN, Birrueta JO, et al. Ensembles of endothelial and mural cells promote angiogenesis in prenatal human brain. Cell 2022;185:3753–69.e18.
29. Winkler EA, Kim CN, Ross JM, Garcia JH, Gil E, Oh I, et al. A single-cell atlas of the normal and malformed human brain vasculature. Science 2022;375:eabi7377.
30. Yang AC, Vest RT, Kern F, Lee DP, Agam M, Maat CA, et al. A human brain vascular atlas reveals diverse mediators of Alzheimer's risk. Nature 2022;603:885–92.
31. Zheng Y, de la Cruz CC, Sayles LC, Alleyne-Chin C, Vaka D, Knaak TD, et al. A rare population of CD24(+)ITGB4(+)Notch(hi) cells drives tumor propagation in NSCLC and requires Notch3 for self-renewal. Cancer Cell 2013;24:59–74.
32. Yang ZF, Ho DW, Ng MN, Lau CK, Yu WC, Ngai P, et al. Significance of CD90+ cancer stem cells in human liver cancer. Cancer Cell 2008;13:153–66.
33. Tang KH, Dai YD, Tong M, Chan YP, Kwan PS, Fu L, et al. A CD90+ tumor-initiating cell population with an aggressive signature and metastatic capacity in esophageal cancer. Cancer Res 2013;73:2322–32.
34. Jin S, Guerrero-Juarez CF, Zhang L, Chang I, Ramos R, Kuan C-H, et al. Inference and analysis of cell-cell communication using CellChat. Nat Commun 2021;12:1088.
35. Menke JR, Raleigh DR, Gown AM, Thomas S, Perry A, Tihan T. Somatostatin receptor 2a is a more sensitive diagnostic marker of meningioma than epithelial membrane antigen. Acta Neuropathol 2015;130:441–3.
36. Kopan R, Ilagan MXG. The canonical Notch signaling pathway: unfolding the activation mechanism. Cell 2009;137:216–33.
37. Bray SJ. Notch signalling in context. Nat Rev Mol Cell Biol 2016;17:722–35.
38. Bray SJ. Notch signalling: a simple pathway becomes complex. Nat Rev Mol Cell Biol 2006;7:678–89.
39. Snyder JM, Shofer FS, Van Winkle TJ, Massicotte C. Canine intracranial primary neoplasia: 173 cases (1986–2003). J Vet Intern Med 2006;20:669–75.
40. Joutel A, Corpechot C, Ducros A, Vahedi K, Chabriat H, Mouton P, et al. Notch3 mutations in CADASIL, a hereditary adult-onset condition causing stroke and dementia. Nature 1996;383:707–10.
41. Tournier-Lasserve E, Joutel A, Melki J, Weissenbach J, Lathrop GM, Chabriat H, et al. Cerebral autosomal dominant arteriopathy with subcortical infarcts and leukoencephalopathy maps to chromosome 19q12. Nat Genet 1993;3:256–9.
42. Siegenthaler JA, Ashique AM, Zarbalis K, Patterson KP, Hecht JH, Kane MA, et al. Retinoic acid from the meninges regulates cortical neuron generation. Cell 2009;139:597–609.
43. Siegenthaler JA, Choe Y, Patterson KP, Hsieh I, Li D, Jaminet S-C, et al. Foxc1 is required by pericytes during fetal brain angiogenesis. Biol Open 2013;2:647–59.
44. Zarbalis K, Siegenthaler JA, Choe Y, May SR, Peterson AS, Pleasure SJ. Cortical dysplasia and skull defects in mice with a Foxc1 allele reveal

the role of meningeal differentiation in regulating cortical development. Proc Natl Acad Sci U S A 2007;104:14002–7.
45. Choe Y, Siegenthaler JA, Pleasure SJ. A cascade of morphogenic signaling initiated by the meninges controls corpus callosum formation. Neuron 2012;73:698–712.
46. Fre S, Hannezo E, Sale S, Huyghe M, Lafkas D, Kissel H, et al. Notch lineages and activity in intestinal stem cells determined by a new set of knock-in mice. PLoS ONE 2011;6:e25785.
47. Muzumdar MD, Tasic B, Miyamichi K, Li L, Luo L. A global double-fluorescent Cre reporter mouse. Genesis 2007;45:593–605.
48. Kalamarides M, Stemmer-Rachamimov AO, Niwa-Kawakita M, Chareyre F, Taranchon E, Han Z-Y, et al. Identification of a progenitor cell of origin capable of generating diverse meningioma histological subtypes. Oncogene 2011;30:2333–44.
49. Nguyen MP, Seo K, Eaton CD, Lucas C-HG, Chen WC, Choudhury A, et al. A case (report) for mechanistic validation of meningioma molecular therapies. Neurooncol Adv 2022;4:vdac162.
50. Giovannini M, Robanus-Maandag E, van der Valk M, Niwa-Kawakita M, Abramowski V, Goutebroze L, et al. Conditional biallelic Nf2 mutation in the mouse promotes manifestations of human neurofibromatosis type 2. Genes Dev 2000;14:1617–30.
51. Tsai JC, Goldman CK, Gillespie GY. Vascular endothelial growth factor in human glioma cell lines: induced secretion by EGF, PDGF-BB, and bFGF. J Neurosurg 1995;82:864–73.
52. Lee WH. Characterization of a newly established malignant meningioma cell line of the human brain: IOMM-Lee. Neurosurg 1990; 27:389–95.
53. Püttmann S, Senner V, Braune S, Hillmann B, Exeler R, Rickert CH, et al. Establishment of a benign meningioma cell line by hTERT-mediated immortalization. Lab Invest 2005;85:1163–71.
54. Wu Y, Cain-Hom C, Choy L, Hagenbeek TJ, de Leon GP, Chen Y, et al. Therapeutic antibody targeting of individual Notch receptors. Nat 2010;464:1052–7.
55. Wei K, Korsunsky I, Marshall JL, Gao A, Watts GFM, Major T, et al. Notch signalling drives synovial fibroblast identity and arthritis pathology. Nature 2020;582:259–64.
56. Magill ST, Vasudevan HN, Seo K, Villanueva-Meyer JE, Choudhury A, John Liu S, et al. Multiplatform genomic profiling and magnetic resonance imaging identify mechanisms underlying intratumor heterogeneity in meningioma. Nat Comms 2020;11:4803.
57. Long DM. Vascular ultrastructure in human meningiomas and schwannomas. J Neurosurg 1973;38:409–19.
58. Bousquet Mur E, Bernardo S, Papon L, Mancini M, Fabbrizio E, Goussard M, et al. Notch inhibition overcomes resistance to tyrosine kinase inhibitors in EGFR-driven lung adenocarcinoma. J Clin Invest 2020;130:612–24.
59. Varga J, Nicolas A, Petrocelli V, Pesic M, Mahmoud A, Michels BE, et al. AKT-dependent NOTCH3 activation drives tumor progression in a model of mesenchymal colorectal cancer. J Exp Med 2020; 217:e20191515.
60. Choy L, Hagenbeek TJ, Solon M, French D, Finkle D, Shelton A, et al. Constitutive NOTCH3 signaling promotes the growth of basal breast cancers. Cancer Res 2017;77:1439–52.
61. Vasudevan HN, Braunstein SE, Phillips JJ, Pekmezci M, Tomlin BA, Wu A, et al. Comprehensive molecular profiling identifies FOXM1 as a key transcription factor for meningioma proliferation. Cell Rep 2018;22:3672–83.
62. Krebs LT, Xue Y, Norton CR, Sundberg JP, Beatus P, Lendahl U, et al. Characterization of Notch3-deficient mice: normal embryonic development and absence of genetic interactions with a Notch1 mutation. Genesis 2003;37:139–43.
63. Buch T, Heppner FL, Tertilt C, Heinen TJAJ, Kremer M, Wunderlich FT, et al. A Cre-inducible diphtheria toxin receptor mediates cell lineage ablation after toxin administration. Nat Methods 2005;2:419–26.
64. Butler A, Hoffman P, Smibert P, Papalexi E, Satija R. Integrating single-cell transcriptomic data across different conditions, technologies, and species. Nat Biotechnol 2018;36:411–20.
65. Stuart T, Butler A, Hoffman P, Hafemeister C, Papalexi E, Mauck 3rd WM, et al. Comprehensive integration of single-cell data. Cell 2019;177:1888–902.e21.
66. Hafemeister C, Satija R. Normalization and variance stabilization of single-cell RNA-seq data using regularized negative binomial regression. Genome Biol 2019;20:296.
67. Tirosh I, Izar B, Prakadan SM, Wadsworth MH, Treacy D, Trombetta JJ, et al. Dissecting the multicellular ecosystem of metastatic melanoma by single-cell RNA-seq. Science 2016;352:189–96.
68. Kline CN, Joseph NM, Grenert JP, van Ziffle J, Talevich E, Onodera C, et al. Targeted next-generation sequencing of pediatric neuro-oncology patients improves diagnosis, identifies pathogenic germline mutations, and directs targeted therapy. Neuro Oncol 2017;19:699–709.